

# Enhancing the Production of Eco-Friendly Silk Fabrics through the Application of Nonthermal Plasma Wettability Techniques

Ahmed Rida Galaly\* and Nagia Dawood



Cite This: *ACS Omega* 2024, 9, 20791–20806



Read Online

ACCESS |



Metrics & More

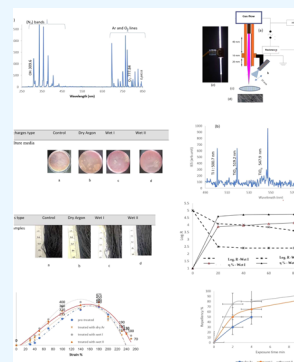


Article Recommendations



Supporting Information

**ABSTRACT:** The combination of the effects of nonthermal plasma using atmospheric pressure of plasma jet and the photocatalytic effects of titanium dioxide nanoparticles was used to study the plasma flow modes, electrical characteristics, nonthermal characteristics, antimicrobial measurements, and surface modifications. Using different wettabilities of argon discharges in a laminar flow: (i) wet I, wettability with 2.4 slm argon mixture with oxygen ratio  $O_2$ , equivalent to 15 mslm ( $Ar/O_2$ ), and (ii) wet II, wettability ( $Ar/O_2$ ) mixture combined with titanium dioxide, to accelerate the inactivation process on the nonwoven fabric surface. For wet 0, wet I, and wet II discharges, the average rate of heat transfer to the nonwoven silk fabric increased significantly. Specifically, it goes from 104.6 to 118.6 and then to 241.7 mW, respectively. The kinetic deactivation rate of *Escherichia coli* increases starting at 0.20, then going up to 0.32, and finally reaching  $0.57 \text{ min}^{-1}$ . The increased wettability of the  $TiO_2$  photocatalyst results in an enhanced bactericidal rate, which is caused by both the heat impact from the nonthermal jet and potentially photocatalytic disinfection, leading to the generation of active species. The mechanical parameters owing to different wettabilities and plasma interactions with the fabric membrane were tested for the treated samples, such as stiffness, ultimate yield strength, tensile strength, strain, hardening, elongation, resilience, and toughness.



## 1. INTRODUCTION

A novel method for studying the effects of plasma on various applications can be achieved through a combination of low gas temperature, low pressure, and atmospheric pressure glow discharge in air. This method has been explored in many studies, which have investigated the effects of heat-induced reactive species and ultraviolet (UV) radiation,<sup>1–3</sup> bacterial genera, and surface disinfection by atmospheric pressure air-generated plasmas.<sup>4</sup> To further understand the atmospheric pressure of plasma generated in air and its interaction with microorganisms, all necessary diagnostic techniques have been outlined.<sup>5</sup> Additionally, research has been conducted to examine the role of cold plasmas in biological and environmental applications.<sup>6,7</sup>

Atmospheric pressure nonthermal plasma generated in the air directly accelerates the disinfection process of microbes attached to any surface without causing any damage.<sup>8</sup> When the nonthermal plasma impinges directly in the air onto the contaminated sample, the ability to eliminate bacterial adhesion to the surfaces is 100 times greater than with indirect jet application, owing to the efficiency of the disinfection process and the direct delivery of charges to contaminated surfaces.<sup>9</sup> The disinfection process is affected by various parameters such as ozone, UV radiation, plasma, neutral active species, and hydroxyl radicals.<sup>10</sup>

Fabric is a polymer that plays an important role in daily life and is one of the most important industries in the world.<sup>11</sup> Fabric has many applications, such as house clothing, medical surgical gowns, and agricultural fabrics. In recent years, the production of multifunctional fabrics has received increasing

attention worldwide.<sup>12,13</sup> Nanoparticles with excellent properties, such as titanium dioxide, silver, zinc oxide, and copper, have been introduced in many fields.<sup>14</sup> Depending on their size and morphology, titanium dioxide nanoparticles possess unique properties such as electrical and thermal conductivity, photocatalytic activity, and antibacterial properties while being nontoxic to human cells.<sup>15</sup>

The use of cold plasma as an environmentally friendly physical agent is a topic of growing research interest in the field of modern fabric technology, particularly in regard to environmental requirements. From an ecological and economic perspective, cold plasma is an acceptable choice,<sup>16,17</sup> where the exposure to atmospheric pressure plasma (APPJ) causes physical and chemical changes in the surface or near-surface layers of fabric materials. Reactive species generated in the APPJ glow discharge play a crucial role in modern technological processes that emphasize environmental sustainability.

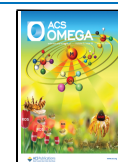
Due to the high efficiency of plasma technology in industrial applications, besides the low environmental impact and simplicity, it is currently widely used in various environmental processes, such as the application of cold plasma by APPJ to

Received: November 7, 2023

Revised: April 20, 2024

Accepted: April 24, 2024

Published: May 3, 2024



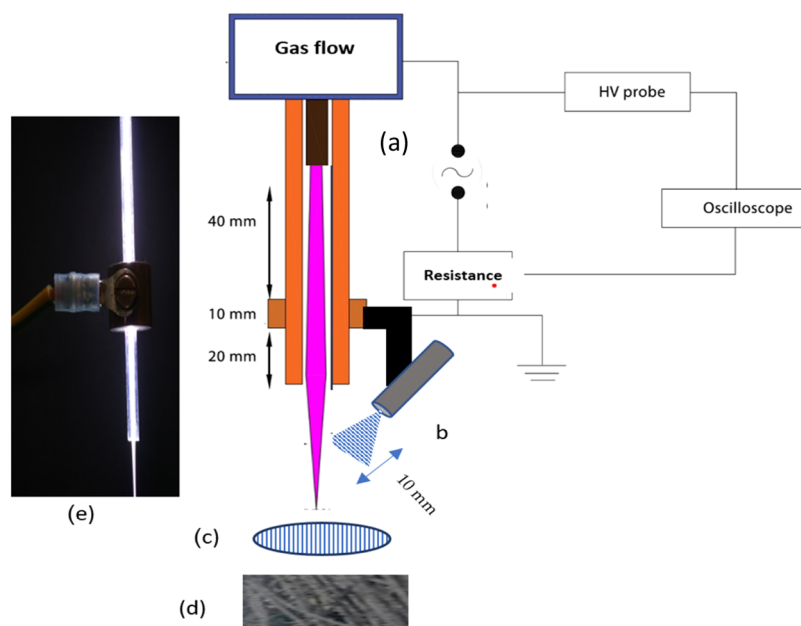


**Figure 1.** (a) APPJ experimental setup, (b)  $\text{TiO}_2$  precursor spray rate tester with an atomizer, (c) mesh control, (d) nonwoven sample, and (e) APPJ image contains the ground electrode for calculating plasma jet dimensions as a calibration scale.

living organisms attached to fabrics. Cold plasma is a safe process for both electrical and biological applications,<sup>18</sup> where it is used for the surface treatment of materials to bring about changes in material properties. The textile industry is advancing the use of plasma technology for diverse purposes, such as ensuring dimensional stability, enhancing resistance to ultraviolet degradation, self-cleaning capabilities, offering antibacterial qualities, and flame repellency.<sup>19</sup>

The titanium dioxide ( $\text{TiO}_2$ ) photocatalyst, as a light-induced antibacterial agent, has attracted great attention and interest in the fabric industry owing to its excellent photoreactivity, chemical stability, lack of toxicity, and other advantages, as well as its physicochemical properties. At wavelengths less than 400 nm, the recombination of electrons and holes is known to occur within nanoseconds when titanium dioxide is exposed to ultraviolet light, thereby increasing the effectiveness of antimicrobial agents in determining the type of microorganism.<sup>20,21</sup>

*Escherichia coli*, referred to as *E. coli*, is a Gram-negative bacterium frequently found in both natural and artificial environments. This versatile microorganism comprises a diverse group, with certain strains being harmless and others potentially posing a threat to human health. Illnesses caused by *E. coli* can manifest in a range of symptoms, including diarrhea, respiratory, and urinary tract infections.<sup>22</sup> The influence of plasma on various bacterial genera is a recent development made possible by a low gas temperature and atmospheric pressure. There have been numerous studies conducted on the evaluation of UV rays and reactive species caused by heat,<sup>23</sup> as well as methods of surface disinfection using atmospheric pressure air-generated plasmas.<sup>24</sup> Various diagnostic techniques have been employed to investigate the interaction between atmospheric pressure plasma and microbes.<sup>25</sup> Additionally, research has been conducted on the role of cold plasmas in biological and environmental applications.<sup>26</sup>

Many studies have dealt with nonthermal plasmas in air generated by plasma jets at atmospheric pressure (APPJ). Many parameters affect the disinfection of microorganisms attached to

fabric surfaces, such as survival curves, different gas mixtures, distances between the beam of APPJ and fabric samples, different beam intensities, different applied voltages, and different types of grounded meshes (aluminum and copper) covered with fabric samples containing microbes.<sup>27</sup> In addition, the use of different distances between the grid lines of the meshes acts as an indirect exposure process using different concentrations of pure argon and different mixtures of  $\text{O}_2/\text{Ar}$  plasma discharges, different sources of the magnetic field, and direct and indirect exposure times.<sup>28</sup> Other parameters, such as the spectroscopic and photographic characteristics of non-thermal plasmas in air generated by (APPJ), and the mechanical parameters of the fabric, such as tensile strength, elongation, hardness, frictional resistance, and light transmittance,<sup>29</sup> are also discussed.

Millions of pilgrims visit the city of Makkah (Mecca) every year in the Hajj and Umrah seasons and touch the Kabba (the holy house of Muslims), which is covered with the cloth Kiswa and is made of silk fabric.<sup>30,31</sup> Hence, microbes are spread, and it poses a great challenge to eliminate them and to produce antimicrobial fabrics for Kiswa to prevent contamination.

Many publications cover very rich applications of nanotechnology and plasma technology in the fabric industry, especially in the disinfection of microbes and the killing of microorganisms attached to fabric.<sup>32,33</sup> Many researchers have studied the subject of glow discharge plasmas at atmospheric pressure owing to technically simple systems: no need for vacuum systems, more supply gas options, and cost-effectiveness.

In a recent study, the plasma characteristics of APPJs were experimentally studied. A plume of cold plasma emitted by the APPJ acted to produce an antimicrobial coating as a protective silk fabric in combination with  $\text{TiO}_2$  as a photocatalytic antibacterial agent, injected into the APPJ, or arising from the nebulizer spray.

## 2. MATERIALS AND METHODS

**2.1. APPJ Experimental Setup.** Figure 1a shows the full experimental setup used for the APPJ to apply the nonthermal effect and to investigate the antibacterial properties of the nonwoven silk sample (n-WSF) from the Kiswa represented by Figure 1d.<sup>34</sup> The APPJ was powered from a high-voltage AC source, and to control the circuit's current, a sinusoidal AC signal was supplied to the top copper ring through a 33 k $\Omega$  resistor, with a variable frequency of up to 60 kHz and a voltage between 2.5 and 25 kV. Discharges were created using wet argon (wet I—oxygen/argon admixture), with argon flow rates between 0.4 and 4 slm (standard liters per minute), and oxygen admixture equal to 15 mslm. In addition, a Tektronix P6015A grounded high-voltage probe was connected to the lower ring to allow a 350 MHz digital oscilloscope to evaluate the electrical properties of the jet's ejected plume and the applied voltage. The light emitted by the APPJ was captured by a lens at the end of a fiber optic cable using an Avaspec-2048 spectrometer with a CCD detector to determine the axial distribution of optical emission spectroscopy from the nozzle beam to the bacterial colony samples in the n-WSF. A mass flow meter (Alicat Scientific Model No. 20 SLPm-D) was used to measure the wet I flow rate, and a thermometer was used to measure the mean plasma gas temperature (Luxtron Corporation, Model No. 604).

The plasma plume emerges from the APPJ, which has an inner diameter of 1.5 mm and is distributed over a large area of the n-WSF samples by indirect exposure using a grounded aluminum mesh controller configuration (8 holes per inch of hole width, 3 mm), as shown in Figure 1c. Photocatalytic titanium dioxide (TiO<sub>2</sub>) nanoparticles (MVX solution, Hi-tech, Kitakyushu, Japan), representing wet II, combined with the emerging argon/oxygen jet, representing wet I, were placed 10 mm from the jet outlet for the inactivation process of culture media of *E. coli* (*E. coli*—Gram-negative bacilli) attached to n-WSF.<sup>35</sup> A TiO<sub>2</sub> precursor spray tester with an atomizer to control the flow rate of wet II is shown in Figure 1b. Furthermore, a TiO<sub>2</sub> solution is used for the wetting process at a concentration with a value of 0.5 g per liter to the n-WSF sample. Finally, Figure 1e shows a photo of the ground electrode, including the afterglow of the emerging plasma beam. The beam-size calibration processes are briefly discussed; see the SM.

**2.2. Water Repellency Tester.** Water repellency is a characteristic that pertains to a fabric's resistance to wetting. However, the protection against water is not entirely effective under high hydrostatic pressure. Consequently, the wearer may become wet in heavy rain when the hydrostatic pressure is sufficiently high.

Enhancing the performance and quality of silk fabric through treatment with APPJ discharge will be introduced and evaluated at various treatment exposure times (*t*) and under different nonthermal plasma conditions, including dry, wet I, and wet II. The experimental results of the water repellency test for the n-WSF repellency of the untreated and plasma-treated samples are shown in Figure 2 (Standard International Group, Hong Kong Limited). This evaluation involved determining the percentage of water repellency (waterproofness) of the n-WSF using drops of water at room temperature from a syringe containing 250 mL of water. The drops were ejected from a nozzle diameter of 6.3 mm, positioned 150 mm away from the fabric sample, which was mounted on an inclined holder at a 45° angle. After 25 s, the amount of water remaining on the fabric was measured.<sup>36,37</sup>

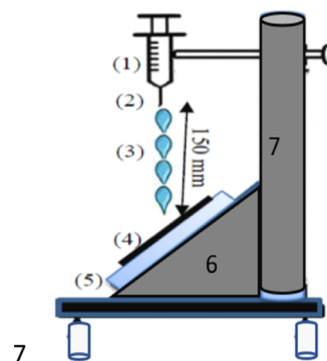


**Figure 2.** Water repellency test for n-WSF repellency of the untreated and plasma-treated samples containing (1) a syringe, (2) a jet nozzle, (3) water drop, (4) a fabric sample, (5) a support inclined with 45°, (6) a holder, and (7) a stand.

**2.3. Tensile and Elongation Tester.** Using the Zweigle Z010 model conforming to ASTM D412–98a, we measured the tensile and elongation behaviors of n-WSF in Kiswa samples that were pretreated and treated with nonthermal plasma from the APPJ plume. The measurements were conducted at a tension speed of 100 mm/min according to ASTM D412–98a. The average values obtained from three separate measurements indicate the results. The stress  $\sigma$  (kPa), strain  $\epsilon$  (percent), and Young's modulus (stiffness) values represent the basic mechanical parameters. Subsequently, there were other parameters such as the ultimate yield strength, tensile strength, hardening, elongation, resilience, and toughness behaviors.<sup>38,39</sup> The samples were compared with three different plasma configurations: dry argon, wet I discharges, and wet II discharges.

**2.4. Culture Media Preparation.** Experimental evaluation of antimicrobial characteristics of n-WSF samples obtained from Kiswa was conducted using the inactivation process of *E. coli* (*E. coli*—Gram-negative bacilli) attached to the samples. Various nonwoven silk samples were employed, and the following tests were conducted to determine their efficiency: first, we prepared an overnight culture of approximately 10<sup>5</sup> cell-forming units per milliliter (cfu/mL) of *E. coli* using untreated n-WSF samples as control Petri dishes that were not exposed to the APPJ plume. Second, we assessed the antimicrobial performance of the n-WSF samples after treatment with a viable suspension of culture media for different exposure times. Finally, we spread *E. coli* onto a series of Petri dishes containing MacConkey agar medium (Oxoid Australia, Adelaide, SA) to evaluate the results. From the 15 n-WSF samples, five samples were exposed to dry Ar discharges, five samples were exposed to wet I discharges, five samples were exposed to wet II discharges at different exposure times, and for each run, one was kept as a control and not exposed.

The bacterial reduction, measured as the logarithm of the CFU/mL (colony-forming units per milliliter) of bacterial colonies attached to the n-WSF samples before and after the antibacterial process using APPJ, was evaluated using a control group of Petri dishes with a known concentration of 10<sup>5</sup> CFU/mL *E. coli*.<sup>40–42</sup> The inactivation rate, which depends on the plasma exposure time, was calculated using eq 1.<sup>43</sup> The plates were exposed to wet I or wet II wettability, and the results were compared to the control group

**Table 1. Research Plan for the Development of an Antimicrobial Controller by APPJ Measurements**

dry argon discharge	experimental studies of n-WSF using APPJ	plasma flow modes	(a) $V-I$ waveform (b) jet velocity and plasma spot diameter (c) jet length and width	antimicrobial controller by APPJ
wet I discharge		electrical characteristics	(a) jet power (b) consumed energy	
wet II discharge		nonthermal characteristics	(a) jet temperature (b) amount of heat transfer	
		antimicrobial measurements	(a) survival curves of <i>E. coli</i> (b) deactivation kinetic rate of bacteria	
		surface modification	(a) surface morphology (b) repellency quality (c) mechanical properties	

$$\log(R) = \log_{10} \left[ \frac{N_0}{N} \right] \quad (1)$$

The concentration of bacteria before and after plasma treatment can be expressed as  $N_0$  and  $N$ , respectively, in colony-forming units (CFU) per milliliter. The inactivation rate,  $\eta$ , can be determined using eq 2

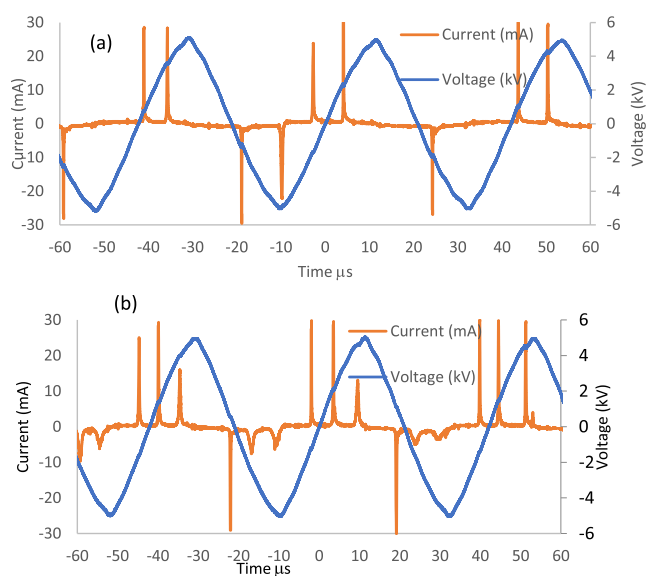
$$\text{inactivation rate } \eta = \left[ \frac{N_0 - N}{N} \right] \times 100\% \quad (2)$$

Table 1 shows the research plan for the development of an antimicrobial controller that utilizes APPJ measurements, by studying the plasma flow modes, electrical characteristics, nonthermal characteristics, antimicrobial measurements, surface modifications, and performance quality. Furthermore, the treatment efficacy, exposure duration, water repellency property, mechanical parameters, and heat directly impacted nonwoven silk fabric (from Kiswa samples), using combined effects of nonthermal plasma at an atmospheric pressure of plasma jet in the laminar flow, and photocatalytic using titanium dioxide, at an atmospheric pressure of plasma jet, with different wettabilities of argon discharge: (i) dry argon (wet 0), (ii) wettability I (wet I); with 2.4 standard liter per minute argon admixture with oxygen ratio  $O_2$ , equivalent to 15 milli-standard liter per minute, and (iii) wettability II (wet II); ( $Ar/O_2$ ) admixture combined with titanium dioxide, sprayed with ratio 0.5 g per liter into the jet, to produce antimicrobial coating as protective n-WSF.

### 3. RESULTS AND DISCUSSION

**3.1. Plasma Flow Modes.** Two methods will be discussed to determine the plasma flow modes and to determine the suitable characteristics, measurements, and antimicrobial application of laminar flow mode for different nonthermal plasma wettabilities to improve the antimicrobial properties of n-WSF, as a green approach as follows.

**3.1.1. Voltage–Current Waveform of APPJ Discharge.** Figure 3a,b shows the discharge wettability effect on voltage–current signals, where wet I of oxygen 15 mslm, with an argon flow rate of 2.4 and 2.6 slm, respectively, changes in the stability of APPJ waveforms. For each signal, the measured applied voltage is sinusoidal with a peak-to-peak voltage ( $U$ , kV) of 11.51 kV, while the discharge current ( $I$ , mA) consists of the displacement current as short peaks, represented by a current pulse of 2.6 slm (as shown in Figure 3b), more than 2.4 slm (as shown in Figure 3a), appearing at each half-cycle when the plasma is formed.<sup>44</sup> This may be due to



**Figure 3.** Voltage and current waveforms of wet I discharges (argon–oxygen admixture) for an argon flow rate of (a) 2.4 slm and (b) 2.6 slm.

1. More sheath around the nozzle as the argon flow rate increased to more than 2.4 slm.
2. The gas discharge residence time in the discharge zone reaches a maximum at a gas flow rate of 2.4 slm and decreases as the gas flow rate is more than 2.4 slm.

For a flow rate of 2.6 slm, there is a ripple in the elapsed closed area of the corresponding charge–voltage ( $Q-V$ ) Lissajous characteristics,<sup>45</sup> using a 40 kV high-voltage capacitor with a capacity of 15 nF attached to the APPJ experimental setup to measure power consumption. It was connected between the lower electrode and the ground. ( $Q-V$ ) Lissajous characteristics as shown in Figure 4b, in contrast for 2.4 slm homogeneous elapsed closed Lissajous figure (almond shape), as shown in Figure 4a. The shape of the ( $Q-V$ ) Lissajous figure gradually changes with an increase in the flow rate exceeding 2.4 slm.

3. The transition from laminar to turbulent flow as the flow rate increases from 2.4 to 2.6 slm.

**3.1.2. Jet Velocity and Plasma Spot Diameter.** For a given type of fluid, the laminar or turbulent flow mode can be defined using the Reynolds equation<sup>46,47</sup> as follows

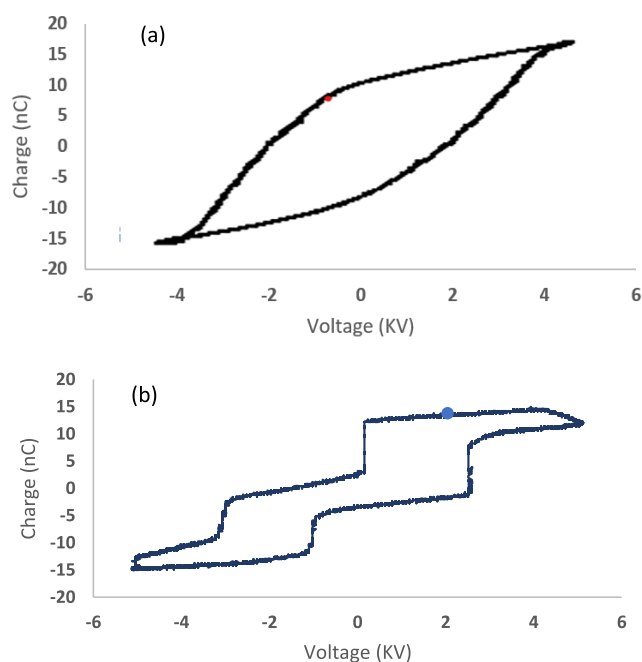


**Figure 4.** Charge–voltage ( $Q$ – $V$ ) Lissajous characteristics of wet I discharges (argon–oxygen admixture) for an argon flow rate of (a) 2.4 slm and (b) 2.6 slm.

$$Re = \left( \frac{4 \times 10^{-4}}{6\pi} \right) \times \left( \frac{\rho}{\mu} \right) \times \left( \frac{Q}{D} \right) \quad (3)$$

where  $Re$  is the Reynolds number,  $\rho$  ( $\text{kg}/\text{m}^3$ ) is the gas density,  $Q$  ( $\text{m}^3/\text{s}$ ) is the gas volume flow rate,  $\mu$  ( $\text{kg}/\text{m s}$ ) is the gas dynamic viscosity, and  $D$  (m) is the hole diameter (inner diameter of the nozzle tube), as shown in Table 2 for wet I.

**Table 2.** Reynolds Number Parameters for Wet I

15 mslm $\text{O}_2$	1 slm Ar	units	parameters
1.35	1.449	$\text{kg}/\text{m}^3$	density $\rho$
$1.5 \times 10^{-3}$	$1.5 \times 10^{-3}$	m	nozzle diameter $D$
$2.022 \times 10^{-5}$	$2.1 \times 10^{-5}$	$\text{kg}/\text{m s}$	dynamic viscosity $\mu$
$1.52 \times 10^{-5}$	$1.265 \times 10^{-5}$	$\text{m}^2/\text{s}$	kinematic viscosity
$2.5 \times 10^{-7}$	$\text{Arslm} \times 1.6667 \times 10^{-5}$	$\text{m}^3/\text{s}$	flow rate $Q$

According to eq 2, and Table 2, the Reynolds number ( $Re$ ) increases as the wet I discharge flow rate ( $Q$ ) increases from 0.4 to 4 slm, admixed with a constant value of 15 mslm  $\text{O}_2$  (according to our previous research [Galaly et al.<sup>42</sup>], 15 mslm represents the optimal oxygen admixture for the inactivation process using an atmospheric pressure plasma jet with wet argon discharges). Furthermore, the jet velocity  $v$  as a function of the flow rate for wet I discharge according to eq 4a or 4b is

$$v = \left( \frac{Q}{A} \right) \quad (4a)$$

$$Re = \left( \frac{\rho}{\mu} \right) \times D \times v \quad (4b)$$

where  $A$  is the sectional area of the nozzle.

Figure 5 shows, for the flow rate represented by region I from 0.4 up to 2.4 slm, the velocity values increased from 3.8 up to 28.7 m/s, the plasma jet spot diameter was increased from 0.25

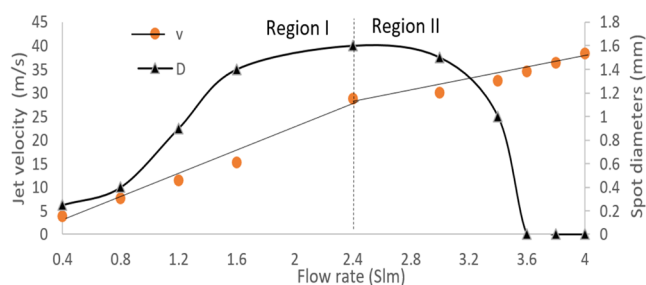


**Figure 5.** Jet velocity and plasma spot diameters as a function of the flow rate for the wet argon discharge flow rate from 0.4 to 4 slm, admixed with 15 mslm  $\text{O}_2$ .

up to 1.6 mm (spot diameters measured using the diameter dimension of the ground electrode hole calibration of the APPJ images as discussed in the SI), and the flow is mainly laminar with a stable streamline flow where adjacent layers smoothly flow over each other equivalent to  $Re$  equal to 2333. Additionally, for the flow rate represented by region II after the dashed line from 2.4 up to 4 slm, the velocity values increased from 28.7 up to 38.3 m/s, and the plasma jet's spot diameter decreased from 1.6 mm and began to disappear, where the flow is mainly changed from a laminar flow to random motion and turbulent flow mode, leading to more dissipated energy and the consumed energy begins to decrease as will be discussed in Section 3.2. As indicated, the plasma jet has two modes. The laminar flow mode is present when  $Re$  is below 2333 and transforms to the turbulent flow mode when the gas flow exceeds 2.4 slm.

**3.1.3. Jet Length and Width.** A dimension calibration method (using Microsoft Paint, Windows 10) was used to calibrate the APPJ images; see the (SI). The ground electrode was used as a calibration scale to determine the width and length of the beam for the afterglow of the emerging jet. Figure 6a,b

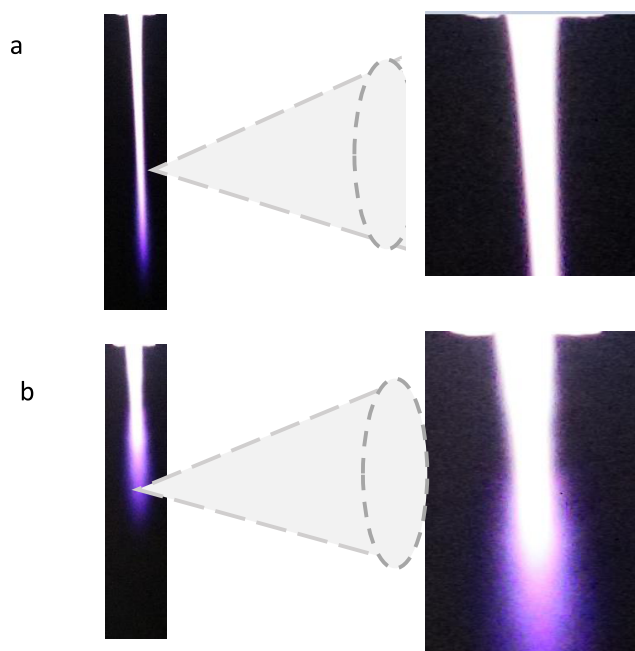


**Figure 6.** Photoimaging of wet I discharge for (a) an Ar flow rate of 2 slm as the laminar flow mode and (b) an Ar flow rate of 3.2 slm as the turbulent flow mode.

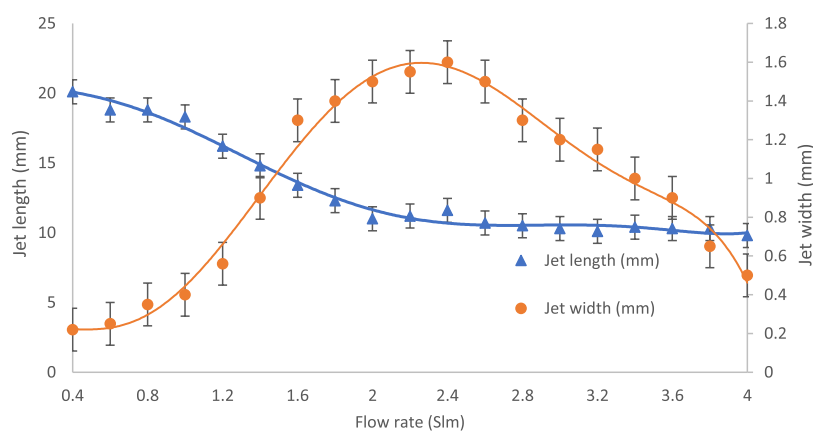


**Figure 7.** Plasma jet dimensions as a function of flow rate for the wet argon discharge flow rate from 0.4 to 2.4 slm, admixed with 15 mslm O<sub>2</sub>.

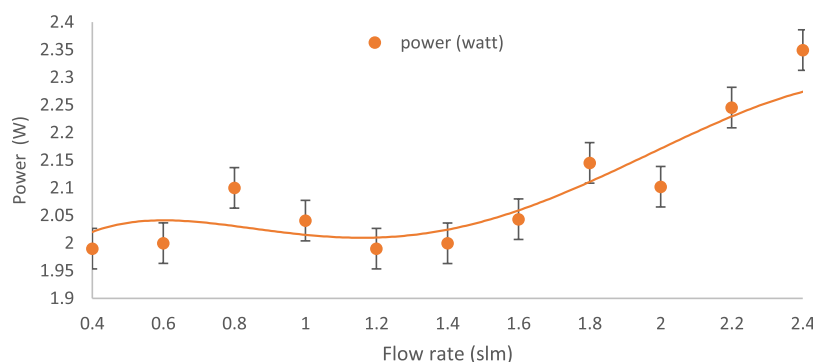


**Figure 8.** Emerging jet power (watt) as a function of the influence of wet I flow rate (standard liter per minute).

shows photographs of the APPJ discharge taken in a darkened laboratory with a Canon digital camera. Figure 6 show photoimaging of the APPJ discharge wettability with O<sub>2</sub> ratios equal to 15 mslm for

1. Wet I discharge with an Ar flow rate of 2 slm as an example for the laminar flow mode, and
2. Wet I discharge with an Ar flow rate of 3.2 slm as an example for the turbulent flow mode.

Figure 6 indicates the existence of two modes: when the flow rate exceeds more than 2.4 slm, the mode changes into turbulence, causing the radial spread of the plasma jet.

Figure 7 shows the beam size as a function of the flow rate for wet I discharge. The jet length drops from 20.1 mm at 0.4 slm to 11.6 mm at 2.4 slm with more decrement to 9.8 mm at 4 slm, while the width mainly increases from 0.4 mm at 0.4 slm to 1.6 mm at 2.4 slm and began to decrease to 0.5 mm at 4 slm. This may be attributed to more discharge in the downstream region, indicating that the afterglow discharge in the laminar flow mode from 0.4 slm reaches 2.4 slm. Furthermore, the width values started to decrease in the turbulent flow mode when the flow rate exceeded more than 2.4 slm because of the discharge distribution between the downstream region outside the tube and the upstream region inside the inner diameter of the tube.<sup>48</sup> This may seem to contradict the previously established<sup>49</sup> that when the plasma jet operates in the laminar mode, the disruption of the surrounding air entering the plasma jet is minimal and is only marginally influenced by its speed. In this state, the flow rate increased in the jet length. However, as the transition to turbulence occurs, the mixing effect diminishes the length of the jet, and in the turbulent mode, the transport mechanisms become more dominant. Our explanation for this apparent

discrepancy may be due to more arc and sheath formation around the nozzle in addition to a greater number of current peaks behind the maximal laminar flow mode.

**3.2. Electrical Characteristics.** **3.2.1. Jet Power and Consumed Energy.** The power  $P$  and frequency  $F$  of the APPJ discharge can be obtained using the voltage–current waveform in Figure 3 and the following equation as in (eq 5)<sup>50</sup>

$$P = F \int_t^T U(t)I(t)dt \quad (5)$$

Inside the laminar flow mode discharge, which is characteristic of homogeneous emerging plasma, before the transition from laminar to turbulent flow. Figure 8 shows the effect of wet I flow rate (standard liter per minute) of different argon flow rates from 0.4 to 2.4 slm on the emerging jet power (watt), where the jet power increases from 1.95 to 2.34 W.

Additionally, two methods were used to estimate the energy consumed by the APPJ plasma:

1. As shown in Figure 9, the amount of consumed energy ( $\epsilon$ ) can be calculated by dividing the power of the discharge plasma (which was calculated from Figure 8's estimate) by the frequency tuned to 25 kHz (which was calculated from Figure 3's estimate of the  $I-V$  waveform).
2. The enclosed area of the ( $Q-V$ ) Lissajous figure (which was calculated from Figure 4's estimate) according to eq 6

$$E(L) = F \int Q dV = A \text{Lissajous} \quad (6)$$

where  $V$  is the applied voltage, and  $Q$  is the quantity of transported charges, which changes with the applied voltage.

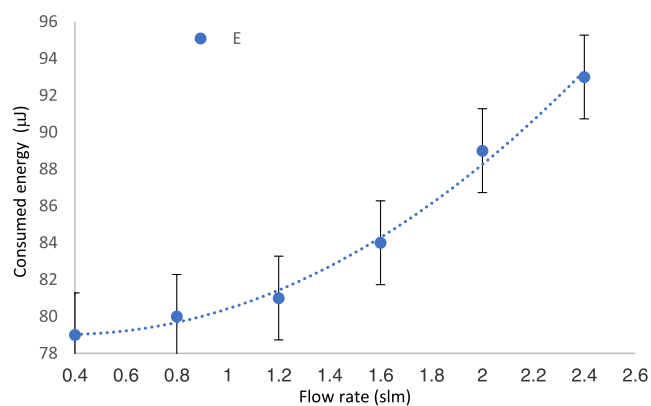


**Figure 9.** Consumed energy as a function of the flow rate for the wet argon discharge flow rate from 0.4 to 2.4 slm, admixed with 15 mslm O<sub>2</sub>.

For laminar flow, the flow velocity, jet velocity, and energy consumed are low, showing a stable streamlined flow and smooth flow between adjacent layers. The consumed energy ( $\epsilon$ ) increases from 79  $\mu\text{J}$  at 0.4 slm to 95  $\mu\text{J}$  at 2.4 slm, when  $Re$  increases above the value of 2300, and transitions from laminar to turbulent mode occur, with high velocity and gas flow; ( $\epsilon$ ) starts to decrease after 2.4 slm. The wettability by wet I (Ar: 2 slm/O<sub>2</sub>: 15 mslm) was chosen in our project because it represents the maximal laminar flow mode of the plasma jet and a low number of current peaks, in addition to reducing sheath formation around the jet.<sup>51</sup>

The increase in jet power and energy consumption as the discharge current increases may be attributed to the increase in carrier loss resulting from the growth of APPJ plasma volume with an increasing discharge current. As the APPJ plume completely enveloped and occupied the discharge gap between the nozzle and the sample, the discharge current density escalated with additional increases in the discharge current. The increase in current density led to an increase in electron density, which, in turn, resulted in a higher loss of charge carriers (diffusion and recombination). These losses in discharge carriers were compensated for by the increase in the power and energy dissipated in the discharge.

### 3.3. Nonthermal Characteristics. 3.3.1. Jet Temperature.

The measured jet temperature reached (n-WSF) samples with Reynolds numbers under the maximum laminar flow mode value. Figure 10 shows the influence of the flow rate from 0.4 to 2.4 slm on the measured jet temperatures ( $T_j$ ), which can be classified as follows:<sup>52</sup>

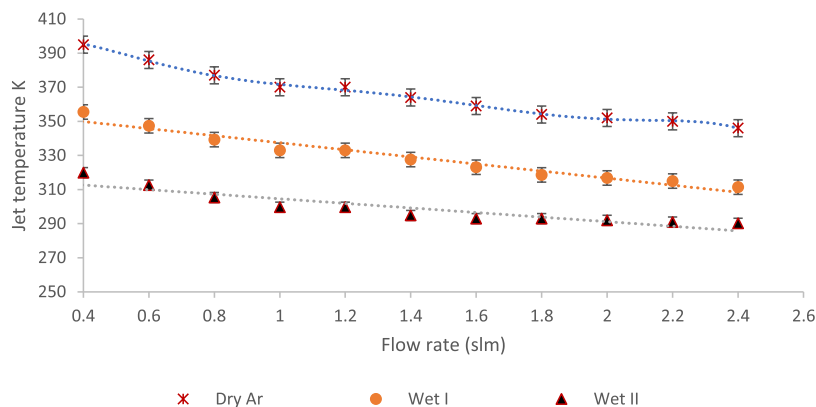
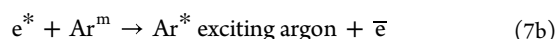
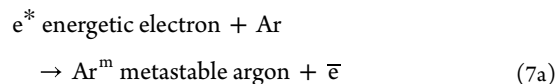


**Figure 10.** Flow rate from 0.4 to 2.4 slm on the jet temperatures for dry and different wet argon discharges.

- (i) Dry argon discharge: the Ar plume interacted with ambient gases and molecules in a dry argon discharge, resulting in a decrease in the jet temperature. At a flow rate of 0.4 slm, the temperature ( $T_j$ ) of dry argon was 395 K, which decreased to 346 K at 2.4 slm. The excited Ar species and high-energy electrons in the plasma interact with ambient air



- (ii) Wet I discharge: (Ar/O<sub>2</sub>) with 2 slm argon admixture with oxygen ratio O<sub>2</sub>, equivalent to 15 mslm, where jet temperatures decrease from 355 K at 0.4 slm to 311 K at 2.4 slm occurs, where ( $T_j$ )<sub>wet I</sub> decreases more than ( $T_j$ )<sub>dry argon</sub>. High-energy electrons in the plasma as well as excited argon species may contribute to the interaction of ambient air and lead to additional reactions.<sup>53</sup>

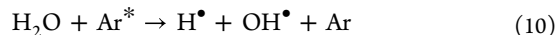
- (a) Energetic electrons ( $e^*$ ) react with argon (Ar) to produce metastable Ar ( $\text{Ar}^m$ )



- (b) Energetic electron reacts with  $\text{Ar}^m$  to generate exciting argon ( $\text{Ar}^*$ )



- (c) Exciting argon ( $\text{Ar}^*$ ) combines with water to produce  $\text{OH}^*$ , with the radicals  $\text{O}^*$  and  $\text{OH}^*$  released as a result of air entering the discharge zone or impurities in the gas



and



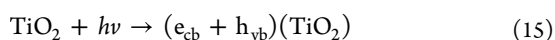
- (d) Ambient air interacts with excited N<sub>2</sub> species and high-energy electrons in the plasma as follows





- (iii) Wet II discharge: combined wet I with titanium dioxide, sprayed with a ratio of 0.5 g/L into the jet; for a wet argon temperature, a lowering from 319 K at 0.4 slm to 291 K at 2.4 slm occurs, where  $(T_j)_{\text{wet II}} < (T_j)_{\text{wet I}} < (T_j)_{\text{dry argon}}$ . The Ar/O<sub>2</sub> admixture creates additional reactions when light is absorbed by TiO<sub>2</sub>, along with other reactions that were previously mentioned, whereby increasing the wettability II dosage, a photon from the nonthermal plasma jet in addition to TiO<sub>2</sub> photocatalysis, and the band gap of TiO<sub>2</sub> is overcome by APPJ photons, resulting in increased energy that creates additional electron–hole pairs as follows:

- (a) Absorption of energy from APPJ photons owing to the incident light of the nonthermal jet<sup>54</sup>

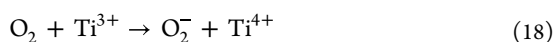


and

- (b) Photons emitted from the APPJ can overcome the band gap of TiO<sub>2</sub> to produce more active substances that can be absorbed by cells, accelerating the inactivation rate process<sup>55,56</sup>



and



where  $e_{\text{cb}}$  is a conduction band electron,  $h_{\text{vb}}$  is a valence band hole, and  $\text{Ti}^{2+}$ ,  $\text{Ti}^{3+}$ , and  $\text{Ti}^{4+}$  are the titanium oxidation states.

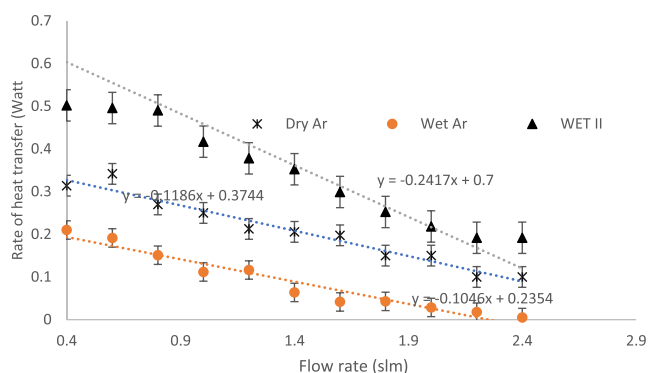
**3.3.2. The Amount of Heat Transfer.** The amount of heat transfer  $Q_{\text{H}}$  [Watt] onto (n-WSF) samples is a very important parameter for producing antibacterial *kiswa* samples. Using Newton's law of heat transfer, the heat loss  $Q_{\text{H}}$  by the APPJ is calculated as the forced convection heat loss through the laminar mode flow and can be represented by eq 17<sup>57,58</sup>

$$Q_{\text{H}} = 0.664Pr^{0.3}Re^{0.5}\frac{\sigma_a}{L}A\Delta T \quad (19)$$

$$\text{where, } Pr = \frac{\eta C_p}{\sigma_a} \quad (20)$$

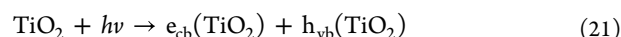
$Pr$  (dimensionless) represents the Prandtl number,  $\eta$  (kg/m s) is the gas dynamic viscosity,  $C_p$  (J/kg K) is the specific heat,  $\sigma_a$  watt/m K is the thermal conductivity, and  $Pr$  is (22.77 and 0.70) for argon and oxygen, respectively. Considering the Reynolds number  $Re$  in the laminar flow mode,  $A$  is the area of the discharge volume [m<sup>2</sup>], and  $L$  is the length of the discharge volume (nozzle) [m]. The thermal conductivity  $\sigma_a$  is [0.016 and 0.024 W/m K] for argon and oxygen, respectively, and  $\Delta T$  is the change in temperature between the  $T_j$  and the ambient temperature (290 K) in the laminar mode ( $T_j$  estimated from Figure 10 for dry argon, wet I, and wet II).

Figure 11 shows the heat impacting onto the (n-WSF) samples  $Q_{\text{H}}$  as a function of the laminar flow rate,  $Q_{\text{H}}$  is straight lines, with an average value of 104.6 mW for Ar<sub>dry</sub>, 118.6 mW for wet I, and 241.7 mW for wet II; the attached bacterial colonies on n-WSF samples are directly impacted by this heat, where ( $Q_{\text{H}}$ ) increases for wet I and wet II discharges more than for dry argon discharge. This can be attributed to the following reasons:



**Figure 11.** Heat impact on the bacterial colonies attached as a function of flow rate in the laminar mode discharge for dry and wet argon.

- (i) For wet I discharge as shown in Figure 12a, where the measured optical emission spectra for the emerging jet of APPJ, with the lines and bands representing wavelengths, ranging from 200 to 850 nm, show from the intensity emission spectra (IES), that besides there is a hydroxyl band (OH) at 309.6 nm ( $(A^2\Sigma^+ - X^2\Pi)$  transition), oxygen (O) radical lines at {777.84 and 843.8 nm}- ( $3s^23p^5(^2P^{\circ}_{3/2})4s$  transition), where reactive species radical emission OH<sup>•</sup> and O<sup>•</sup> represent the power agents, which increase ( $Q_{\text{H}}$ ), and then the process by which bacteria are microbially inactivated.<sup>59,60</sup>
- (ii) For wet II discharge as shown in Figure 12b, where the measured OES of the atomic Ti I and molecular lines TiO<sub>2</sub>, for wet II, combined with OES of wet I discharge at an 11.2 mm axial distance from the nozzle and admixture at 2.4 slm Ar and 15 mslm O<sub>2</sub>. As using wet II, a TiO<sub>2</sub> photocatalyst was added to the reactions. The titanium dioxide band gap is overcome by a fraction of the energy from the APPJ plume, leading to the creation of electron–hole (e–h) pairs. Photons are used as representations to establish these pairings<sup>61–63</sup>



Electron–hole (e–h) pairs result in the formation of more active chemicals that may be absorbed by the germs, enhancing sterilizing effectiveness, where  $e_{\text{cb}}$  is an electron in the conduction band and  $h_{\text{vb}}$  is a hole in the valence band. In addition,  $Q_{\text{H}}$  includes impact parameters for the inactivation effect because the type of active particles produced depends on the plasma ionization level.

The previous measurements, nonthermal, electrical, and optical emission spectroscopy characteristics of APPJ, represent the roadmap for antimicrobial and surface modification measurements using the measured parameters: applied voltage, 11.2 KV; frequency, 25 KHz; power, 2.2 W; jet length, 11.3 mm; jet width, 1.5 mm; and energy, 89 mJ]. as follows.

**3.4. Antimicrobial Measurements.** **3.4.1. Survival Curves of *E. coli*.** Based on the 11 nonwet samples, five of them were exposed to wet I discharge, five were exposed to wet II discharges at varying exposure times, and one was designated as a control and not exposed. In light of the fact that the preparation of the bacterial colony samples and the survival curves of *E. coli* for dry argon were previously investigated in our work,<sup>64</sup> and the bacterial concentration was determined to be approximately 10<sup>5</sup> cell-forming units per milliliter (CFU/mL) of *E. coli* (*E. coli*),<sup>65,66</sup> it is now feasible to evaluate the bacterial

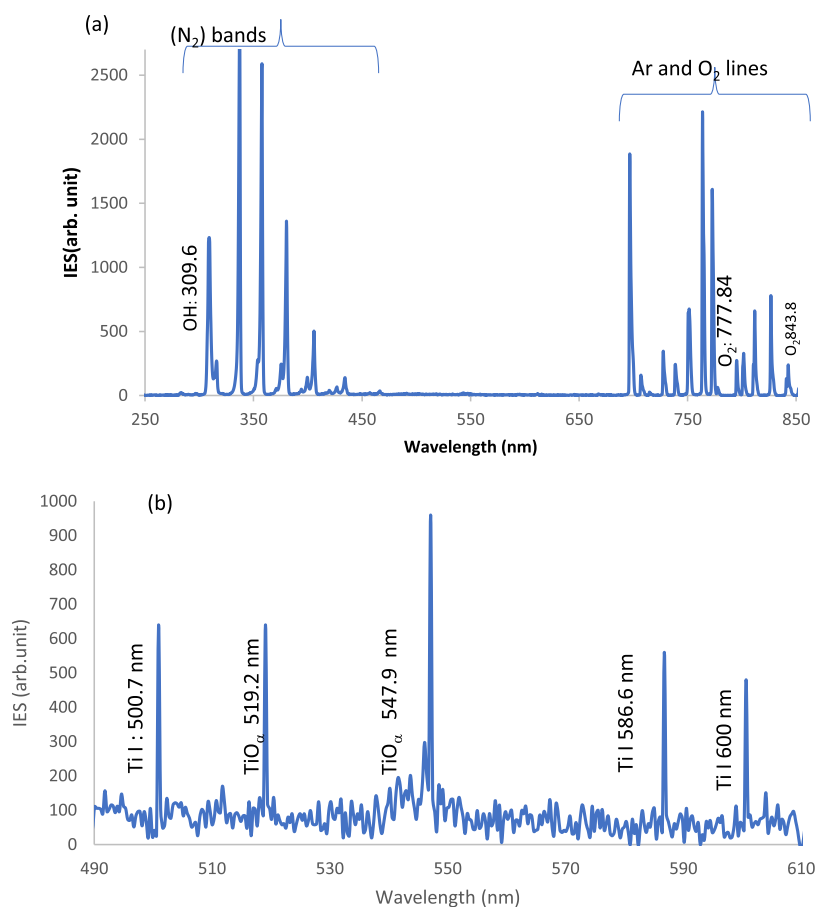


**Figure 12.** (a) (OH) bands and O radical lines, as OES for wet I discharge, and panel (b) represents atomic Ti I, and molecular lines TiO<sub>α</sub>, as OES for wet II coupled with wet I discharge, at an 11.2 mm axial distance from the nozzle, and admixture at 2.4 slm Ar and 15 mslm O<sub>2</sub>.

colony concentrations of *E. coli* (CFU/mL) before and after treatment.

Figure 13 displays a graph illustrating the logarithmic reduction of bacterial count (CFU/mL) and the inactivation

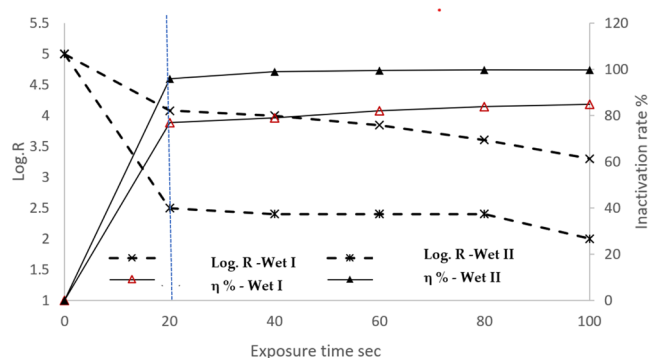


**Figure 13.** Logarithm of the bacterial reduction  $R$  (CFU/mL) and inactivation rate  $\eta$  % at different wettabilities: wet I and wet II discharges as a function of the exposure time.

rate (%) in relation to exposure time for different wettabilities, specifically, wet I and wet II discharges. As exposure time increased, so did the bacterial inactivation process, as shown in eqs 1 and 2. The plasma jet inactivation results can be roughly divided into two time periods, as shown in Table 3: 0–20 and 20–100 s. The inactivation process experienced a moderate increase before the dotted line for the logarithmic reduction  $R$ ,

**Table 3. Wettability Comparison between Wet I and Wet II for the Logarithm of  $R$  and  $\eta$  (%) Values for the Discharge Wettabilities I and II at Various Exposure Times**

period (s)		wet I	wet II
0–20	log( $R$ )	4.1	2.5
	$\eta$ %	77	96
100	log( $R$ )	3.2	2.1
	$\eta$ %	88	99

and a hyperincrease after the dotted line for the inactivation rate  $\eta$  %.

The wettability comparison between wet I and wet II shows that the logarithmic  $R$  and  $\eta$  (%) values for wet II are higher than those for wet I at different exposure times. This may be attributed to the combined effect of the photocatalytic disinfection effect<sup>67</sup> of wet II due to the wettability by NPs such as TiO<sub>2</sub>, with the nonthermal effect of APPJ, which speeds up the inactivation percentage  $\eta$  %.

**3.4.2. Deactivation Kinetic Rate of Bacteria.** The results of the survival curves showed that the bacterial reduction process and inactivation rate increased with longer exposure times for the n-WSF samples to the APPJ plume.<sup>68–70</sup> Figure 14a displays the controller sample photo, while Figure 14b–d depicts the photographs of n-WSF Kiswa samples with varying applied discharge controller factors, namely, dry argon, wet I, and wet II. Additionally, Figure 15a presents the control Petri dish before treatment, containing the bacterial colony concentration of *E. coli* (CFU/mL), and Figure 15b–d portrays the *E. coli* culture

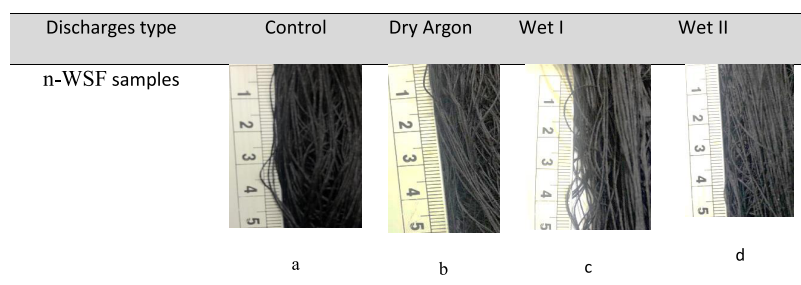


**Figure 14.** (a) The controller sample image, while panels (b–d) illustrate then-WSF Kiswa samples with varying discharge controllers, including dry argon, wet I, and wet II, respectively.

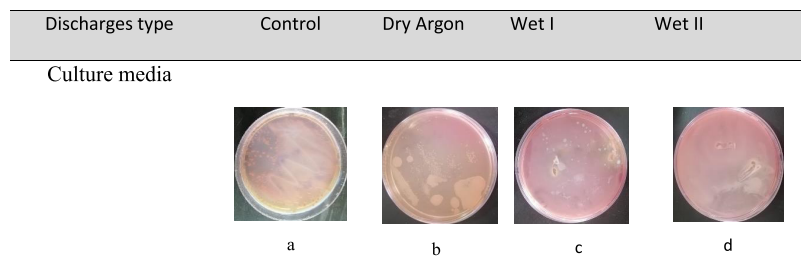


**Figure 15.** (a) The bacterial colony concentration of *E. coli* (CFU/mL) before and after treatment in a control dish and examination of the *E. coli* culture media after exposure to different discharge controllers (b–d).

media exposed to different discharge controllers. The inactive regions inside the Petri dish are illustrated by an etched area and grow using the discharge controller factors, dry argon, wet I, and wet II, respectively.

The Weibull deactivation function for the kinetic rate of bacteria ( $\kappa$ ) is a very important parameter for the comparison between the sterilization rates of different types of wettability discharges and can be driven<sup>71–73</sup> as follows

$$N_t/N_0 = e^{-kt} \quad (22)$$

Then

$$k = \left( \frac{t}{\ln\left(\frac{N_0}{N_t}\right)} \right) \quad (23)$$

where  $N_0$  and  $N_t$  are the concentrations of live *E. coli* cells at the start ( $t = 0$ ) and end of treatment ( $t$ ), respectively.

Figure 16 shows  $\ln\left(\frac{N_0}{N_t}\right)$  as a function of the exposure time of dry argon, wet I, and wet II discharges for (n-WSF), exhibiting straight lines with slope  $k$ , represented by  $y = kx$ , where  $k$  increases for wet II with a maximum exposure time of 180 s,

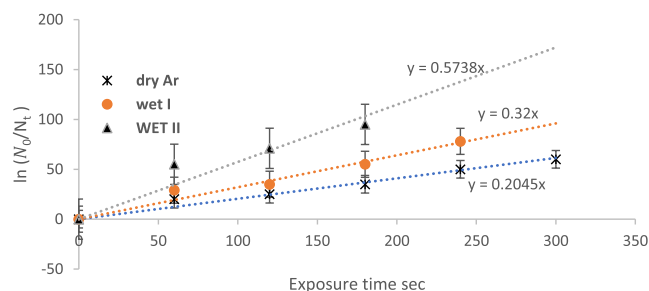


**Figure 16.**  $\ln N_0/N_t$  as a function of the exposure time for dry argon, wet I, and wet II discharges.

lower than those of  $(k)_{\text{dry argon}}$  and  $(k)_{\text{wet I}}$  with 240 and 300 s, respectively. The values of  $(k)$  are 0.20, 0.32, and 0.57  $\text{min}^{-1}$ , corresponding to dry argon, wet I, and wet II, respectively. This means that the bacterial reduction rate increases as the wettability by wet II exceeds that of wet I and dry discharge due to the combined effect of nonthermal plasma using atmospheric pressure of the plasma jet in the laminar flow mode and photocatalysis using titanium dioxide, supporting the results discussed in Section 3.2.

**3.5. Surface Modification.** **3.5.1. Surface Morphology.** Under the same applied conditions of an applied voltage of 11.2 kV and a frequency of 25 kHz, surface morphological changes of n-WSF were examined for different levels of wettabilities (0, I, and II) at flow rates of 2.4 slm for Ar, 15 mslm for  $\text{O}_2$ , and 0.5 g/L for  $\text{TiO}_2$ , respectively. Figure 17a shows the controlled morphology of n-WSF prior to the black dyestuff process. Figure 17b,d illustrates the effect of APPJ treatments, which modify the n-WSF surface topography due to the bombardment of the fabric surface by energetic plasma species. The induced surface morphology changes of the treated n-WSF were dependent on the low-temperature treatment of APPJ using wet 0, wet I, or wet II discharges at various exposure times.<sup>74</sup>

The results of scanning electron microscopy (SEM) revealed that the fabric surfaces became rougher after plasma treatment, and in some instances, voids and cracks were visible, particularly when the wet 0 discharge with the APPJ treatment was used, as demonstrated in Figure 17b.<sup>75</sup> It was also observed that the voids and cracks became more noticeable as the exposure time increased, which was thought to be due to the physical sputtering and chemical etching effects.

Using wet I discharge treatment as shown in Figure 17c, voids and cracks disappeared and increased the surface repellency of n-WSF, probably as exposure time increased. This finding was attributed to the higher ratio of reactive species radical emission ( $\text{OH}^\bullet$  and  $\text{O}^\bullet$ ), which act as power agents, increasing the treatment intensity ( $Q_H$ ) given to the fabric surface and resulting in higher fabric repellency.

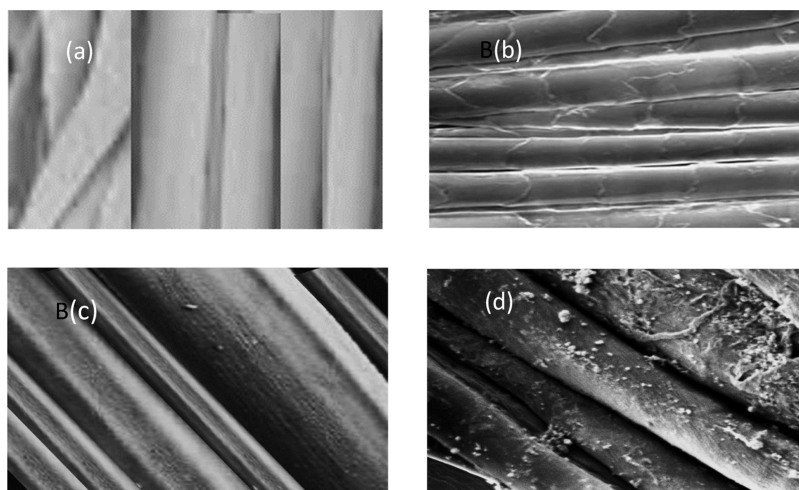


**Figure 17.** Optical scanning microscope images of  $5 \times 5 \mu\text{m}^2$  surface morphological changes of n-WSF samples for (a) control, (b) wet 0 discharge, (c) wet I discharge, and (d) wet II discharge.

Figure 17d shows the morphological changes resulting from the wet II plasma treatment, which involves the synergistic effects of nonthermal plasma, oxygen, and titanium dioxide. These treatments are expected to significantly enhance the repellency of the fabric, as will be discussed in Section 3.5. This improvement may increase the hydrophobic surface barrier of n-WSF, thereby providing additional opportunities for achieving waterproof characteristics in addition to the antimicrobial effect.

**3.5.2. Repellency Quality.** In this section, the performance of different discharges represented by dry argon, wet I, and wet II is compared according to the quality of the repellency of water characteristics of the n-WSF samples.

Figure 18 shows the repellency quality at various exposure time intervals ranging from 0 to 10 min, where various n-WSF

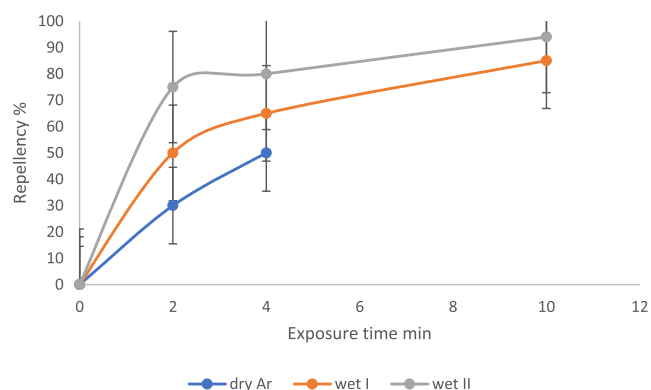


**Figure 18.** Repellency of n-WSF samples (%) as a function of exposure time (minute) for dry argon, wet I, and wet II discharges.

samples were placed under the influence of the measured parameters mentioned previously. In general, the repellency quality increased in all cases as the exposure time increased.<sup>76,77</sup>

Table 4 shows that for dry argon, wet I, and wet II discharges, the repellency quality  $\chi$  of the n-WSF increased from 30% to 50% up to 75%, respectively, after 2 min, and  $\chi$  increased from 50 to 65 up to 80%, respectively, after 4 minutes. Furthermore, after 4 min reaching 10 min, n-WSF began to be damaged by dry argon and began to increase from 85 up to 94% for wet I and wet II, respectively.

This indicates that

**Table 4. Repellency Quality  $\chi$  Values of n-WSF after Different Exposure Times**

discharge type	exposure times		
	120 s	240 s	600 s
wet 0	30%	50%	damage
wet I	50%	65%	85%
wet II	75%	80%	94%

- (i) In wet 0 discharge using glow discharge from APPJ, the chemical and physical properties of the outer monolayer of the generated n-WSF samples are altered by the electronic, vibrational, and rotationally excited species generated by the plasma plume.<sup>78–80</sup>
- (ii) The formation of free radicals on the surface of n-WSF is a result of the breakage of covalent bonds by energetic particles, which is influenced by the oxygen-to-argon ratio  $\text{O}_2$  in wet I discharge. This reaction is in addition to the effect mentioned in (i). The active species in the plasma react with the surface radicals to form reactive functional groups, which have a strong affinity for hydrogen in water. This property is known as hydrophilicity.<sup>81–83</sup>
- (iii) As the concentration of  $\text{TiO}_2$  increased in the wet II discharge, more species emitted light at specific wavelengths, such as atomic line Ti at 500.7, 586.6, and 600 nm and molecular line  $\text{TiO}$  at 547.9 and 519.2 nm. This suggests that more particles reacted with high energy onto the fabric, as described in Section 3.1. Additionally, the addition of  $\text{TiO}_2$  led to the incorporation of hydrophilic groups (carbonyl, carboxyl, hydroxyl, and amino groups) into the n-WSF surface after aging treatment. These polar functional groups orient themselves toward the polymer bulk and can interact with one another to form hydrogen bonds, establishing physical bonds and stability within the surface.<sup>84–86</sup>

**3.5.3. Mechanical Properties.** The mechanical properties (MPs) of the 20 n-WSF samples were evaluated; five samples were selected for each of the four groups: untreated, dry argon, wet I, and wet II. Figure 19 shows the untreated and treated samples exposed to a laminar flow of APPJ glow discharges for testing their MPs.

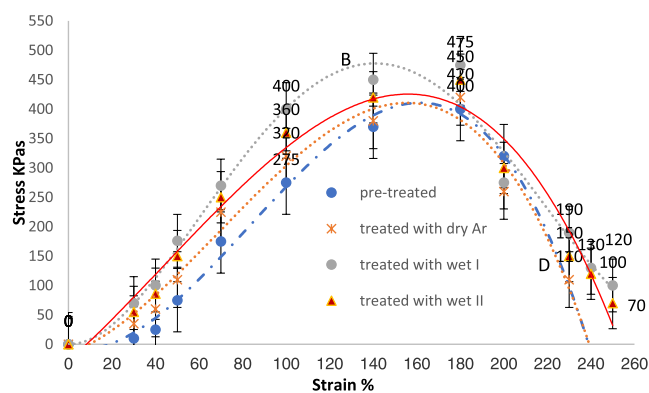


**Figure 19.** Stress as a function of the strain for untreated and treated n-WSF samples with dry argon, wet I, and wet II discharges.

The relationship between stress  $\sigma$  (KPa) and strain  $\epsilon$  percent gives a straight line in the linear region AB, denoted by  $\sigma = E \epsilon$ , with slope  $E$  representing the value of Young's modulus (stiffness),<sup>85</sup> where  $E$  increased, corresponding to values of 2.75, 3.2, 3.6, and 4 KPa in the elastic region.

Tensile resilience ( $RT = \frac{1}{2} \sigma \epsilon$ )<sup>87–89</sup> indicates the area under the curve of the elastic region AB (RT), corresponding to values of 13,750, 16,000, 18,000, and 20,000 J/m<sup>3</sup>. RT represents the ability of the n-WSF sample to absorb energy when elastically deformed by wettability I, and sample II shows a higher capacity than that of the dry argon discharge.

Elongation percentage (%) of the n-WSF samples at breaking point D increases for the wettabilities I and II more than the dry argon discharge, corresponding to values of 200, 230, 240, and 250%.

WT, reported by Microsoft Excel as the area under the curve from the strain–stress curve from A to D to (breakpoint), represents the energy required to extend the length of n-WSF without damage, reflecting the deformation characteristic.<sup>90–92</sup> WT increased to 50,375, 56,275, 70,515, and 65,410 J/m<sup>3</sup>, respectively. All measured MPs of the untreated and treated samples are summarized in Table 5 and are shown below:

- The MPs of treated n-WSF samples under plasma have a positive influence for wettability I (2 slm argon admixture with oxygen ratio O<sub>2</sub>, equivalent to 15 mslm) and wettability II (Ar/O<sub>2</sub> admixture combined with TiO<sub>2</sub>, sprayed with ratio 0.5 g/L into the jet), more than dry argon (100% Ar), and untreated sample.
- The use of APPJ treatment, coupled with wet I and II, on the n-WSF samples increased the elasticity area, stretch, percent strain, and breaking point values.

All previously measured MP data showed that the quality of nonwoven fabric under the influence of different nonthermal plasma wettabilities I and II was superior to the other measured data for fabric pretreated and treated with dry argon, which may be attributed to the plasma wettability discharge, engineered functions by the sputtering characteristics of the jet plume, and polymerization and deposition processes of TiO<sub>2</sub> to induce surface modification and performance quality on n-WSF.<sup>93,94</sup>

**3.6. Antimicrobial Controller by APPJ.** **3.6.1. Laminar Flow Control.** The impact of gas flow as a fluid following the discharge process in the downstream region of the APPJ is explained by using the principles of hydrodynamics. This includes the influence of Reynolds number ( $Re$ ) and gas pressure, as described by Bernoulli's theorem.<sup>95,96</sup>

The velocity of the jet and size of the plasma spots vary based on the flow type, which can be either laminar ( $Re < 2300$ ) or turbulent ( $Re > 2300$ ). When the flow rate is increased, the laminar flow and plasma column length also increase. Paschen's law states that the breakdown voltage of the plasma discharge decreases with increasing flow rate. As a result, the plasma length increases with a higher flow rate at a fixed operation voltage.

In the laminar flow discharge, the diameter of the plasma beam on the substrate surface is smaller than the glass diameter, so mesh control is used to broaden the jet width.

**3.6.2. Mesh Control.** The grounded aluminum mesh as an indirect controller (with eight holes per inch and a hole width of 3 mm) works as an electrode for the APPJ for indirect plasma exposure, with a 4 mm gap over the WST sample. There is a significant rate of heat transfer in the gap region between the mesh and n-WSF despite scattering losses with mesh wires and the largest sheath length surrounding the mesh wires. Owing to the penning effect, significant local electric fields at the Al mesh and considerable heating impact on the antimicrobial process are produced by adequate ionization and excitation processes along the sharp edges of the mesh holes. The Al mesh accelerated charged particles and improved interactions with other particles to form more reactive species, such as OH and O, which increased the killing area of the inactivation process because of the increased electric field between the mesh and the electrodes of the APPJ.<sup>97</sup>

**3.6.3. Wet I Control.** *E. coli* attached to n-WSF was inactivated using a nonthermal APPJ control and a wet I discharge, where the surface of the cell membrane became a collection point for the charged particles produced by APPJ. Depending on how quickly the various coverings represented by coatings, debris, and dead cells erode, an electric field can penetrate the cell membrane. Reactive species, such as O<sub>2</sub> and OH, are the most potent agents influencing the microbial inactivation process of bacteria when the wet I plume interacts with the surrounding gases and molecules.<sup>98</sup>

**Table 5.** Measured Mechanical Properties of the Untreated and Treated n-WSF Samples under Different Discharges: Dry, Wet I, and Wet II Using APPJ

region	parameters	units	untreated	dry Ar	wet I	wet II
from A to B	stiffness	KPa	2.75	3.2	3.6	4
B	yield strength	KPa	275	320	360	400
C	ultimate tensile strength $\sigma_{UTS}$	KPa	410	420	450	475
B–C	strain hardening $\sigma_{UTS} - \sigma_Y$	KPa	135	100	90	125
D	elongation percent at breaking point	%	200	230	240	250
area under the curve of the elastic region	resilience	J/m <sup>3</sup>	13,750	16,000	18,000	20,000
area under the strain–stress curve up to fracture	toughness	J/m <sup>3</sup>	50,375	56,275	70,515	65,410

**3.6.4. Wet II Control.** As the wettability increases because of the coupling between wet I and wet II, the reactive oxygen species, reactive nitrogen species, atomic oxygen, and hydroxyl radicals increase, decreasing the exposure time and accelerating the inactivation process. The disinfecting property of TiO<sub>2</sub> NPs is highly dependent on the photocatalytic effect of TiO<sub>2</sub>,<sup>99</sup> where the outer cell membrane wall of various bacterial species attached to n-WSF acts as a barrier to the wet II mechanism to complete the antibacterial process, so the outer membrane first disintegrates before the whole cells are completely broken down.

According to the photocatalytic oxidization mechanism of Gram-negative *E. coli*, the organic material is oxidized because of its photocatalytic activity, and as a result, the organic material of the cell wall membrane increases the number of holes in the TiO<sub>2</sub> valence band.<sup>100</sup> The bactericidal activity and aggregation of TiO<sub>2</sub> are positively linked to the rate of cell death.<sup>101,102</sup>

#### 4. CONCLUSIONS

The nonthermal, electrical, and optical characteristics of APPJ were discussed, given the improvement in the performance of Kiswa nonwoven silk fabric owing to the combination of the photocatalytic effect of titanium dioxide and the effect of nonthermal plasma. The attachment of living bacteria to the surface covers the nonwoven silk fabric (Kiswa) using wettability I (2 slmad mixed argon with oxygen ratio O<sub>2</sub>, equal to 15 mslm) and wettability II (Ar/O<sub>2</sub> mixture combined with TiO<sub>2</sub>, sprayed in the plasma jet at a ratio of 0.5 g/L) to accelerate the inactivation process. Furthermore, an aluminum mesh was used as an indirect exposure control to increase the antimicrobial area owing to the nonthermal nature of the plasma jet.

The quality of the nonwoven fabric under the influence of different nonthermal plasma wettabilities was improved by studying the surface modification, performance quality, treatment efficiency, exposure time, water repellency property, mechanical parameters, and heat directly impacted on nonwoven silk fabric samples. As the wettability of the TiO<sub>2</sub> photocatalyst increased, the average heat transfer rate, antibacterial treatment, and sterilization rate of the *E. coli* microorganisms increased. This may be due to photocatalytic disinfection and the generation of active species. The sputtering characteristics of the jet plume help the polymerization and deposition processes of TiO<sub>2</sub> induce antimicrobial activity on n-WSF, and wet II accelerates the inactivation process more than wet I discharge. In addition to the influence of the incident cloud of nonthermal jets on the mechanical parameters of the fabric membrane, plasma interactions and wettability are also important. The current article represents a roadmap to improve an environmentally friendly green approach to the nonwoven silk fabric, and our anticipated future work will include nanoparticle solutions with different wetting doses, concentrations, and flow rates for biomedical applications such as surgical instruments to improve the performance of photocatalytic disinfection.

#### ■ ASSOCIATED CONTENT

##### SI Supporting Information

The Supporting Information is available free of charge at <https://pubs.acs.org/doi/10.1021/acsomega.3c08858>.

Photo image of plasma jet dimension calibration method: (S1) for calibrated length, (S2) for calibrated width, (S3) for measured jet length example, and (S4) for measured jet width example (PDF)

#### ■ AUTHOR INFORMATION

##### Corresponding Author

Ahmed Rida Galaly – Department of Engineering Science, Applied College, Umm Al-Qura University, Makkah 24381, Saudi Arabia; [orcid.org/0000-0003-3298-9805](https://orcid.org/0000-0003-3298-9805); Email: [argalaly@uqu.edu.sa](mailto:argalaly@uqu.edu.sa)

##### Author

Nagia Dawood – Physics Department, Faculty of Science, Taibah University, Al Madina Al Monawara 42363, Saudi Arabia

Complete contact information is available at:

<https://pubs.acs.org/10.1021/acsomega.3c08858>

##### Funding

Deanship for Research & Innovation, Ministry of Education in Saudi Arabia for funding this research work through project number: IFP22UQU4250206DSR119.

##### Notes

The authors declare no competing financial interest.

#### ■ ACKNOWLEDGMENTS

The authors extend their appreciation to the Deanship for Research and Innovation, Ministry of Education in Saudi Arabia, for funding this research work through project number IFP22UQU4250206DSR119.

#### ■ ABBREVIATIONS

n-WSF	nonwoven silk fabric
APPJ	atmospheric pressure of plasma jet
NPs	nanoparticles
wet 0	dry argon (100% Ar)
wet I	wettability argon mixture with oxygen (Ar/O <sub>2</sub> )
wet II	wettability (Ar/O <sub>2</sub> ) mixture combined with TiO <sub>2</sub>
TiO <sub>2</sub>	titanium dioxide
<i>E. coli</i>	<i>Escherichia coli</i>
CFU/mL	colonies formed per milliliter
slm	standard liter per minute
mslm	milli-standard liter per minute
MPs	mechanical properties
Kabba	Holey house of Muslims
Kiswa	silk fabric cover of Kabba
green approach	eco-friendly

#### ■ REFERENCES

- (1) Morent, R.; De Geyter, N.; Van Vlierberghe, S.; et al. Deposition of HMDSO-based coatings on PET substrates using an atmospheric-pressure dielectric barrier discharge. *Prog. Org. Coat.* **2009**, *64*, 304–310, DOI: [10.1016/j.porgcoat.2008.07.030](https://doi.org/10.1016/j.porgcoat.2008.07.030).
- (2) Bruggeman, P.; Schram, D.; González, M. Á.; et al. Characterization of a direct dc-excited discharge in water by optical emission spectroscopy. *Plasma Sources Sci. Technol.* **2009**, *18* (2), No. 025017, DOI: [10.1088/0963-0252/18/2/025017](https://doi.org/10.1088/0963-0252/18/2/025017).
- (3) Seo, Y. S.; Mohamed, A.-A. H.; Woo, K. C.; et al. Comparative Studies of Atmospheric Pressure Plasma Characteristics Between He and Ar Working Gases for Sterilization. *IEEE Trans. Plasma Sci.* **2010**, *10*, No. 1109, DOI: [10.1109/tps.2010.2058870](https://doi.org/10.1109/tps.2010.2058870).
- (4) Laroussi, M. Nonthermal decontamination of biological media by atmospheric-pressure plasmas: review, analysis, and prospects. *IEEE Trans. Plasma Sci.* **2002**, *30*, 1409–1415, DOI: [10.1109/TPS.2002.804220](https://doi.org/10.1109/TPS.2002.804220).

- (5) Machala, Z.; Hensel, K.; Akishev, Y. *Plasma for Bio-Decontamination, Medicine and Food Security*; Springer: Netherlands, 2011; p 417.
- (6) Lee, M.-H.; Min, B.; Son, J.; Kwon, T. Influence of Different Post-Plasma Treatment Storage Conditions on the Shear Bond Strength of Veneering Porcelain to Zirconia. *Materials* **2016**, *9*, No. 43, DOI: 10.3390/ma9010043.
- (7) Chen, Z.; Garcia, G.; Arumugaswami, V.; et al. Cold atmospheric plasma for SARS-CoV-2 inactivation. *Phys. Fluids* **2020**, *32*, No. 111702, DOI: 10.1063/5.0031332.
- (8) Bhardwaj, R.; Agrawal, A. Likelihood of survival of coronavirus in a respiratory droplet deposited on a solid surface. *Phys. Fluids* **2020**, *32*, No. 061704.
- (9) Nam, S. H.; Lee, H. J.; Hong, J. W.; Kim, G. C. Efficacy of Nonthermal Atmospheric Pressure Plasma for Tooth Bleaching. *Sci. World J.* **2015**, *2015*, No. 581731, DOI: 10.1155/2015/581731.
- (10) Yan, D.; Wang, Q.; Adhikari, M.; et al. A Physically Triggered Cell Death via Transbarrier Cold Atmospheric Plasma Cancer Treatment. *ACS Appl. Mater. Interfaces* **2020**, *12* (31), 34548–34563, DOI: 10.1021/acsami.0c06500.
- (11) Laroussi, M. Low-Temperature Plasma Jet for Biomedical Applications: A Review. *IEEE Trans. Plasma Sci.* **2015**, *43* (3), 703–712, DOI: 10.1109/TPS.2015.2403307.
- (12) Morent, R.; De Geyter, N.; Leys, C.; et al. Surface Modification of Non-woven Fabric using a Dielectric Barrier Discharge Operating in Air, Helium and Argon at Medium Pressure. *Text. Res. J.* **2007**, *77* (7), 471–488, DOI: 10.1177/0040517507080616.
- (13) De Geyter, N.; Moreno, R.; Leys, C. Surface Modification of a Polyester Non-woven with a Dielectric Barrier Discharge in Air at Medium Pressure. *Surf. Coat. Technol.* **2006**, *201* (6), 2460–2466, DOI: 10.1016/j.surfcoat.2006.04.004.
- (14) Pulgarin, C.; Kiwi, J.; Nadtchenko, V. Mechanism of photocatalytic bacterial inactivation on TiO<sub>2</sub> films involving cell-wall damage and lysis. *Appl. Catal., B* **2012**, *128*, 179–183, DOI: 10.1016/j.apcatb.2012.01.036.
- (15) Gamage, J.; Zhang, Z. Applications of Photocatalytic Disinfection. *Int. J. Photoenergy* **2010**, *2010*, No. 764870, DOI: 10.1155/2010/764870.
- (16) Sunada, K.; Watanabe, T.; Hashimoto, K. Studies on photokilling of bacteria on TiO<sub>2</sub> thin film. *J. Photochem. Photobiol., A* **2003**, *156*, 227–233, DOI: 10.1016/S1010-6030(02)00434-3.
- (17) Ahmed, O. B.; Asghar, A. H.; Bamaga, M.; Bahwerth, F. S.; Ibrahim, M. E. Characterization of aminoglycoside resistance genes in multidrug resistant *Klebsiella pneumoniae* collected from tertiary hospitals during the COVID-19 pandemic. *PLoS ONE* **2023**, *18*, No. e0289359, DOI: 10.1371/journal.pone.0289359.
- (18) de Dicastillo, C. L.; Correa, M. G.; Martínez, F. B. et al. Antimicrobial Effect of Titanium Dioxide Nanoparticles. In *Antimicrobial Resistance - A One Health Perspective*; IntechOpen, 2020.
- (19) He, Z.; Cai, Q.; Fang, H.; et al. Photocatalytic activity of TiO<sub>2</sub> containing anatase nanoparticles and rutile nanoflower structure consisting of nanorods. *J. Environ. Sci.* **2013**, *25*, 2460–2468, DOI: 10.1016/S1001-0742(12)60318-0.
- (20) Romero-Morán, A.; Franco, A. Z.; Sánchez-Salas, J. L.; Méndez-Rojas, M. Á.; Molina-Reyes, J. Electrostatically charged rutile TiO<sub>2</sub> surfaces with enhanced photocatalytic activity for bacteria inactivation. *Catal. Today* **2022**, *392–393*, 154–166.
- (21) Baniya, H. B.; Guragain, R. P.; Baniya, B.; Subedi, D. P. Cold Atmospheric Pressure Plasma Jet for the Improvement of Wettability of Polypropylene. *Int. J. Polym. Sci.* **2020**, *2020*, No. 3860259, DOI: 10.1155/2020/3860259.
- (22) Lagier, J. C.; Edouard, S.; Pagnier, I.; Mediannikov, O.; Drancourt, M.; Raoult, D. Current and past strategies for bacterial culture in clinical microbiology. *Clin. Microbiol. Rev.* **2015**, *28* (1), 208–236, DOI: 10.1128/CMR.00110-14.
- (23) Sun, Y.; Zhang, Z.; Wang, Sh. Study on the Bactericidal Mechanism of Atmospheric-Pressure Low-Temperature Plasma against *Escherichia coli* and Its Application in Fresh-Cut Cucumbers. *Molecules* **2018**, *23* (4), No. 975, DOI: 10.3390/molecules23040975.
- (24) Kirkpatrick, M.; Dodet, B.; Odic, E. Atmospheric pressure humid argon DBD plasma for the application of sterilization - measurement and simulation of hydrogen, oxygen, and hydrogen peroxide formation. *Int. J. Plasma. Environ. Sci. Technol.* **2007**, *1*, 96–101.
- (25) Sarani, A.; Nikiforov, A.; Leys, C. Atmospheric pressure plasma jet in Ar and Ar/H<sub>2</sub>O mixtures: Optical emission spectroscopy and temperature measurements. *Phys. Plasmas* **2010**, *17*, No. 063504.
- (26) Austin, B. The value of cultures to modern microbiology. *Antonie van Leeuwenhoek* **2017**, *110* (10), 1247–1256, DOI: 10.1007/s10482-017-0840-8.
- (27) Jin, D. J.; Uhm, H. S.; Cho, G. Influence of the gas-flow Reynolds number on a plasma column in a glass tube. *Phys. Plasmas* **2013**, *20* (8), No. 083513, DOI: 10.1063/1.4819246.
- (28) Snari, R. M.; Alshahag, M.; Alisaac, A.; Bayazeed, A.; Alsoliemy, A.; Khalifa, M. E.; El-Metwaly, N. M. Smart fabric immobilized with hydrazone probe for colorimetric recognition of bacteria. *J. Mol. Liq.* **2022**, *366*, No. 120149, DOI: 10.1016/j.molliq.2022.120149.
- (29) Alisaac, A.; Alshahag, M.; Alshareef, M.; Snari, R. M.; Alhasani, M.; Abumelha, H. M.; El-Metwaly, N. M. Development of smart cotton fabric immobilized with anthocyanin and potassium alum for colorimetric detection of bacteria. *Inorg. Chem. Commun.* **2022**, *145*, No. 110023, DOI: 10.1016/j.inoche.2022.110023.
- (30) <https://www.dailymail.co.uk/news/article-8575649/Changing-Kiswa-4-5million-silk-cloth-covering-Islams-holy-Kaaba-Mecca-gets-replaced.html>.
- (31) <https://www.arabnews.com/node/2119016/saudi-arabia>.
- (32) Allehyani, E. S. Surface Functionalization of Polyester Fabric for Antibacterial and Antioxidant Properties. *Polymers* **2022**, *14*, No. 5512, DOI: 10.3390/polym14245512.
- (33) Siddiqui, S. I.; Allehyani, E. S.; Al-Harbi, S. A.; Hasan, Z.; Abomuti, M. A.; Rajor, H. K.; Oh, S. Investigation of Congo Red Toxicity towards Different Living Organisms: A Review. *Processes* **2023**, *11*, No. 807, DOI: 10.3390/pr11030807.
- (34) Mohamed, A.-A. H.; Aljuhani, M. M.; Almarashi, J. Q. M.; Alhazime, A. A. The effect of a second grounded electrode on the atmospheric pressure argon plasma jet. *Plasma Res. Express* **2020**, *2* (1), No. 015011, DOI: 10.1088/2516-1067/ab7b36.
- (35) Jiang, H.; Shao, T.; Zhang, C.; et al. Experimental study of Q-V Lissajous Figures in nanosecond-pulse surface discharges. *IEEE Trans. Dielectr. Electr. Insul.* **2013**, *20* (4), 1101–1111, DOI: 10.1109/TDEI.2013.6571423.
- (36) Sharma, N. K.; Misra, S.; Varun; Lamba, R. P.; Choyal, Y.; Pal, U. N. Analysis of Discharge Characteristics of Cold Atmospheric Pressure Plasma Jet. *IEEE Trans. Plasma Sci.* **2021**, *49* (9), 2799–2805, DOI: 10.1109/TPS.2021.3106792.
- (37) Jin, D. J.; Uhm, H. S.; Cho, G. Influence of the gas-flow Reynolds number on a plasma column in a glass tube. *Phys. Plasmas* **2013**, *20* (8), No. 083513, DOI: 10.1063/1.4819246.
- (38) Finnemore, E. J.; Franzini, J. B. *Fluid Mechanics with Engineering Applications*, 10th ed.; McGraw Hill: New York, 2002.
- (39) Viegas, P.; Slikboer, E.; Bonaventura, Z.; et al. Physics of plasma jets and interaction with surfaces: review on modelling and experiments. *Plasma Sources Sci. Technol.* **2022**, *31*, No. 053001, DOI: 10.1088/1361-6595/ac61a9.
- (40) Li, Q.; Li, J.-T.; Zhu, W.-C.; et al. Effect of gas flow rate on the length of atmospheric pressure nonequilibrium plasma jets. *Appl. Phys. Lett.* **2009**, *95*, No. 141502, DOI: 10.1063/1.3243460.
- (41) Laroussi, M. Low Temperature Plasma-Based Sterilization: Overview and State-of-the-Art. *Plasma Processes Polym.* **2005**, *2*, 391–400, DOI: 10.1002/ppap.200400078.
- (42) Asghar, A. H.; Ahmed, O. B.; Galaly, A. R. Inactivation of *E. coli* Using Atmospheric Pressure Plasma Jet with Dry and Wet Argon Discharges. *Membranes* **2021**, *11* (1), No. 46, DOI: 10.3390/membranes11010046.
- (43) Morent, R.; De, N. Inactivation of Bacteria by Non-Thermal Plasmas. In *Biomedical Engineering - Frontiers and Challenges*; IntechOpen, 2011.
- (44) Adhikari, B. C.; Lamichhane, P.; Lim, J. S.; Nguyen, L. N.; Choi, E. H. Generation of reactive species by naturally sucked air in the Ar

- plasma jet. *Results Phys.* **2021**, *30*, No. 104863, DOI: 10.1016/j.rinp.2021.104863.
- (45) Law, V. J.; Milosavljevic, V.; O'Connor, N.; Lalor, J. F.; Daniels, S. Handheld flyback driven coaxial dielectric barrier discharge: Development and characterization. *Rev. Sci. Instrum.* **2008**, *79*, No. 094707.
- (46) Liu, L.-f.; John, B.; Yeung, K. L.; Si, G. Non-UV based germicidal activity of metal-doped TiO<sub>2</sub> coating on solid surfaces. *J. Environ. Sci.* **2007**, *19*, 745–750, DOI: 10.1016/S1001-0742(07)60124-7.
- (47) Horie, Y.; David, D. A.; Taya, M.; et al. Effects of Light Intensity and Titanium Dioxide Concentration on Photocatalytic Sterilization Rates of Microbial Cells. *Ind. Eng. Chem. Res.* **1996**, *35*, 3920–3926, DOI: 10.1021/ie960051y.
- (48) Nwankire, C. E.; Law, V. J.; Nindrayog, A.; Twomey, B.; Niemi, K.; Milosavljevic, V.; Graham, W. G.; Dowling, D. P. Electrical, thermal and optical diagnostics of an atmospheric plasma jet system. *Plasma Chem. Plasma Process.* **2010**, *30*, 537–552, DOI: 10.1007/s11090-010-9236-5.
- (49) Dong, L. F.; Qi, Y. Y.; Zhao, Z. C.; Li, Y. H.; Li, X. C. Study on energy transfer in argon/air in dielectric barrier discharge by optoemission spectra. *Spectrosc. Spectral Anal.* **2008**, *28* (11), 2491–2493.
- (50) “NIST Atomic Spectra Database. <https://www.nist.gov/pml/atomic-spectra-database>, 2020. (last accessed August 21, 2020).
- (51) Wang, W. J.; Yu, Y.; An, T.; et al. Visible-Light-Driven photocatalytic inactivation of *E. coli* K-12 by bismuth vanadate nanotubes: Bactericidal performance and mechanism. *Environ. Sci. Technol.* **2012**, *46*, 4599–4606, DOI: 10.1021/es2042977.
- (52) Fakhouri, H.; Salem, D. B.; Carton, O.; et al. Highly efficient photocatalytic TiO<sub>2</sub> coatings deposited by open air atmospheric pressure plasma jet with aerosolized TTIP precursor. *J. Phys. D: Appl. Phys.* **2014**, *47*, No. 265301.
- (53) Horie, Y.; Masahito, T.; Setsuji, T. Evaluation of Photocatalytic Sterilization Rates of *Escherichia coli* Cells in Titanium Dioxide Slurry Irradiated with Various Light Sources. *J. Chem. Eng.* **1998**, *4*, 577–584, DOI: 10.1252/jcej.31.577.
- (54) Shen, J.; Cheng, C.; Fang, S.; et al. Sterilization of *Bacillus subtilis* Spores Using an Atmospheric Plasma Jet with Argon and Oxygen Mixture Gas. *Appl. Phys. Express* **2012**, *5*, No. 036201, DOI: 10.1143/apex.5.036201.
- (55) Gogniat, G.; Thyssen, M.; Denis, M.; et al. The bactericidal effect of TiO<sub>2</sub> photocatalysis involves adsorption onto the catalyst and the loss of membrane integrity. *FEMS Microbiol. Lett.* **2006**, *258*, 18–24, DOI: 10.1111/j.1574-6968.2006.00190.x.
- (56) Laroussi, M.; Leipold, F. Evaluation of the roles of reactive species, heat, and UV radiation in the inactivation of bacterial cells by air plasma at atmospheric pressure. *Int. J. Mass Spectrom.* **2004**, *233* (1), 81–86, DOI: 10.1016/j.jms.2003.11.016.
- (57) Laroussi, M.; Mendis, D. A.; Rosenberg, M. Plasma interaction with microbes. *New J. Phys.* **2003**, *5*, No. 41, DOI: 10.1088/1367-2630/5/1/341.
- (58) Lu, X.; Naidis, G. V.; Laroussi, M.; et al. Reactive species in non-equilibrium atmospheric-pressure plasmas: Generation, transport, and biological effects. *Phys. Rep.* **2016**, *630*, 1–84, DOI: 10.1016/j.physrep.2016.03.003.
- (59) Verdier, T.; Coutand, M.; Bertron, A.; Roques, C. Antibacterial Activity of TiO<sub>2</sub> Photocatalyst Alone or in Coatings on *E. coli*: The Influence of Methodological Aspects. *Coatings* **2014**, *4*, 670–686.
- (60) Pal, A.; Min, X.; Yu, L. E.; Pehkonen, S. O.; Ray, M. B. Photocatalytic inactivation of bioaerosols by TiO<sub>2</sub> coated membrane. *Int. J. Chem. React. Eng.* **2005**, *3*, No. 14, DOI: 10.2202/1542-6580.1236.
- (61) Jelil, R. A. A review of low-temperature plasma treatment of fabric materials. *J. Mater. Sci.* **2015**, *50*, 5913–5943, DOI: 10.1007/s10853-015-9152-4.
- (62) Morent, R.; De Geyter, N.; Leys, C. Measuring the wicking behavior of fabric by the combination of a horizontal wicking experiment and image processing. *Rev. Sci. Instrum.* **2006**, *77*, No. 093502, DOI: 10.1063/1.2349297.
- (63) Benabbou, A. K.; Derriche, Z.; Felix, C.; Lejeune, P.; Guillard, C. Photocatalytic inactivation of *Escherichia coli*: Effect of concentration of TiO<sub>2</sub> and microorganism, nature, and intensity of UV irradiation. *Appl. Catal., B* **2007**, *76*, 257–263, DOI: 10.1016/j.apcatb.2007.05.026.
- (64) Galaly, A. R.; Zahran, H. H. Inactivation of bacteria using combined effects of magnetic field, low pressure and ultra low frequency plasma discharges (ULFP). *J. Phys.: Conf. Ser.* **2013**, *431*, No. 012014, DOI: 10.1088/1742-6596/431/1/012014.
- (65) Hegemann, D. Plasma polymerization and its applications in fabric. *Indian J. Fiber Text. Res.* **2006**, *31*, 99–115.
- (66) Morent, R.; De Geyter, N.; Verschuren, J.; et al. Non-thermal plasma treatment of fabric. *Surf. Coat. Technol.* **2008**, *202*, 3427–3449.
- (67) Kale, K. H.; Desai, A. N. Atmospheric pressure plasma treatment of fabric using non-polymerising gases. *Indian J. Fiber Text. Res.* **2011**, *36*, No. 288.
- (68) Prat, R.; Shi, M. K.; Clouet, F. Interactions of cold plasmas with polymers and their model molecules: degradation vs. functionalization. *J. Macromol. Sci., Part A* **1997**, *34*, 471–488, DOI: 10.1080/10601329708014974.
- (69) Buyle, G. Nanoscale finishing of fabric via plasma treatment. *Mater. Technol.* **2009**, *24*, 46–51, DOI: 10.1179/175355509X417954.
- (70) Wang, C. X.; Du, M.; Qui, Y. P. Uniformity and penetration of surface modification effects of atmospheric pressure plasma jet into fabric materials. *Adv. Mater. Res.* **2011**, *331*, 356–359, DOI: 10.4028/www.scientific.net/amr.331.356.
- (71) Wang, C. X.; Ren, Y.; Qiu, Y. P. Penetration depth of atmospheric pressure plasma surface modification into multiple layers of polyester fabric. *Surf. Coat. Technol.* **2007**, *202*, 77–83, DOI: 10.1016/j.surfcoat.2007.04.077.
- (72) Finson, E.; Kaplan, S. L.; Wood, L. In *Plasma Treatment of Webs and Films*, 38th Annual Technical Conference Proceedings; Society of Vacuum Coaters: Chicago, 1995.
- (73) Shahidi, S.; Wiener, J.; Ghoranneviss, M. Surface Modification Methods for Improving the Dyeability of Fabric. In *Eco-friendly Fabric Dyeing and Finishing*; Gunay, M., Ed.; InTech: Rijeka, 2013; pp 33–52.
- (74) Qu, Y. Q.; Duan, X. F. Progress, challenge and perspective of heterogeneous photocatalysts. *Chem. Soc. Rev.* **2013**, *42*, 2568–2580.
- (75) Park, H. J.; Nguyen, T. T. M.; Yoon, J.; Lee, C. Role of reactive oxygen species in *Escherichia coli* inactivation by cupric ion. *Environ. Sci. Technol.* **2012**, *46*, 11299–11304.
- (76) Deng, X.; Nikiforov, A. Y.; Coenye, T.; et al. Antimicrobial nano-silver non-woven polyethylene terephthalate fabric via an atmospheric pressure plasma deposition process. *Sci. Rep.* **2015**, *5*, No. 10138.
- (77) Rincón, A.; Pulgarin, C. Photocatalytic inactivation of *E. coli*: effect of (continuous–intermittent) light intensity and of (suspended–fixed) TiO<sub>2</sub> concentration. *Appl. Catal., B* **2003**, *44* (3), 263–284.
- (78) Caballero, L.; Whitehead, K. A.; Allen, N. S.; Verran, J. Inactivation of *Escherichia coli* on immobilized TiO<sub>2</sub> using fluorescent light. *J. Photochem. Photobiol., A* **2009**, *202*, 92–98.
- (79) Grill, A. *Cold Plasma in Material Fabrications*; The Institute of Electrical and Electronics Engineers, Inc.: New York, 1993.
- (80) Badey, J. P.; Espuche, E.; Sage, D.; et al. A comparative study of the effects of ammonia and hydrogen plasma downstream treatment on the surface modification of polytetrafluoroethylene. *Polymer* **1996**, *37* (8), 1377–1386, DOI: 10.1016/0032-3861(96)81135-9.
- (81) Yasuda, H. K. *Plasma Polymerization and Plasma Interactions with Polymeric Materials*; John Wiley and Sons Inc.: New York, 1990.
- (82) Bhatnagar, N. *Plasma Surface Treatment to Enhance Adhesive Bonding* in *Handbook of Adhesive Technology*; Pizzi, A.; Mittal, K. L., Eds.; CRC Press/Routledge Handbooks Online: Boca Raton, 2023.
- (83) Clement, F.; Held, B.; Soulem, N.; Guimon, C. XPS analyses of polystyrene thin films treated under DC pulsed discharges conditions in nitrogen, oxygen and oxygen-argon mixtures. *Eur. Phys. J. Appl. Phys.* **2002**, *18*, 135–151, DOI: 10.1051/epjap:2002035.

(84) Lee, W. Y.; Jin, D. J.; Kim, Y. J.; et al. Characteristics of Plasma Discharge according to the Gas-flow Rate in the Atmospheric Plasma Jets. *J. Korean Vac. Soc.* **2013**, *22* (3), 111–118, DOI: 10.5757/JKVS.2013.22.3.111.

(85) Kim, H. C.; Kim, Y.; Lee, M. K.; et al. Influence of an external electrode on a plasma plume ejected from a syringe electrode inside a glass tube. *J. Korean Phys. Soc.* **2012**, *61*, 557–562, DOI: 10.3938/jkps.61.557.

(86) Tadesse, M. G.; Nagy, L.; Nierstrasz, V.; Loghin, C.; Chen, Y.; Wang, L. Low-Stress Mechanical Property Study of Various Functional Fabric for Tactile Property Evaluation. *Materials* **2018**, *11*, No. 2466, DOI: 10.3390/ma11122466.

(87) Zille, A.; Oliveira, F. R.; Souto, A. P. Plasma Treatment in Fabric Industry. *Plasma Process. Polym.* **2015**, *12*, 98–131, DOI: 10.1002/ppap.201400052.

(88) Roth, J. R. Applications to Nonthermal Plasma Processing. In *Industrial Plasma Engineering*, 1st ed.; CRC Press: Boca Raton, FL, USA, 2001; Vol. 2.

(89) Guimin, X.; Guanjun, Z.; Xingmin, S.; Yue, M.; Ning, W.; Yuan, L. Bacteria Inactivation Using DBD Plasma Jet in Atmospheric Pressure Argon. *Plasma Sci. Technol.* **2009**, *11*, No. 83, DOI: 10.1088/1009-0630/11/1/17.

(90) Morent, R.; De Geyter, N.; Verschuren, J.; De Clerck, K.; Kiekens, P.; Leys, C. Non-thermal plasma treatment of fabric. *Surf. Coat. Technol.* **2008**, *202*, 3427–3449, DOI: 10.1016/j.surfcoat.2007.12.027.

(91) Mai-Prochnow, A.; Murphy, A. B.; McLean, K. M.; Kong, M. G.; Ostrikov, K. K. 2014; Vol. 43, p 508 DOI: 10.1016/j.ijantimicag.2014.01.025.

(92) O'Connor, N.; Cahill, O.; Daniels, S.; Galvin, S.; Humphreys, H. Cold atmospheric pressure plasma and decontamination. Can it contribute to preventing hospital-acquired infections? *J. Hosp. Infect.* **2014**, *88*, 59–65, DOI: 10.1016/j.jhin.2014.06.015.

(93) Alhadrami, H. A.; Shoudri, R. A. M. Titanium Oxide (TiO<sub>2</sub>) Nanoparticles for Treatment of Wound Infection. *J. Pure Appl. Microbiol.* **2021**, *15* (1), No. 437, DOI: 10.22207/jpam.15.1.41.

(94) Nwankire, C. E.; Law, V. J.; Nindrayog, A.; et al. Electrical, thermal and optical diagnostics of an atmospheric plasma jet system. *Plasma Chem. Plasma Process.* **2010**, *30* (5), 537–552, DOI: 10.1007/s11090-010-9236-5.

(95) Kowalski, M.; Salerno-Kochan, R.; Kamińska, I.; Cieślak, M. Quality and Quantity Assessment of the Water Repellent Properties of Functional Clothing Materials after Washing. *Materials* **2022**, *15*, No. 3825, DOI: 10.3390/ma15113825.

(96) Ozcan, G. Performance Evaluation of Water Repellent Finishes on Woven Fabric Properties. *Text. Res. J.* **2007**, *77* (4), No. 265, DOI: 10.1177/0040517507080619.

(97) Chen, M.; Deng, X.; Guo, R.; Fu, C.; Zhang, J. Tensile Experiments and Numerical Analysis of Fabric-Reinforced Lightweight Engineered Cementitious Composites. *Materials* **2022**, *15*, No. 5494, DOI: 10.3390/ma15165494.

(98) Mazumder, N.; Mandal, S.; Agnew, R. J.; Petrova, A.; Boorady, L. M.; Song, G. Characterizing the Tensile Strength of the Fabric Used in Firefighters' Bunker Gear under Radiant Heat Exposure. *Polymers* **2022**, *14*, No. 296, DOI: 10.3390/polym14020296.

(99) Hedges, A. J. Estimating the precision of serial dilutions and viable bacterial counts. *Int. J. Food Microbiol.* **2002**, *76* (3), 207–214, DOI: 10.1016/S0168-1605(02)00022-3.

(100) Franco-Duarte, R.; Černáková, L.; Kadam, S.; et al. Advances in Chemical and Biological Methods to Identify Microorganisms—From Past to Present. *Microorganisms* **2019**, *7* (5), No. 130, DOI: 10.3390/microorganisms7050130.

(101) Singh, M. K.; Ogino, A.; Nagatsu, M. Inactivation factors of spore-forming bacteria using low-pressure microwave plasmas in an N<sub>2</sub> and O<sub>2</sub> gas mixture. *New J. Phys.* **2009**, *11*, No. 5027, DOI: 10.1088/1367-2630/11/11/115027.

(102) Karnopp, J.; Magaldi, B.; Sagás, J.; Pessoa, R. The Effect of Excited Species on the Collisional Energy of Argon Inductively Coupled Plasmas: A Global Model Study. *Plasma* **2022**, *5*, 30–43.